GEOPHYSICS

Seafloor geodesy unveils seismogenesis of large subduction earthquakes in Mexico

Víctor M. Cruz-Atienza[1]*, Josué Tago[2], Luis A. Domínguez[1], Vladimir Kostoglodov[1], Yoshihiro Ito[3], Efraín Ovando-Shelley[4], Tonatiuh Rodríguez-Nikl[5], Renata González[4], Sara Franco[1], Darío Solano-Rojas[2], Joel Beltrán-Gracia[2], Paulina Miranda-García[2], Frédérick Boudin[6], Luis Rivera[7], Anne Bécel[8], Carlos Villafuerte[1], Jorge Real[1], Ekaterina Kazachkina[1], Arturo Ronquillo[9]

Based on measurements of near-trench deformations of the oceanic and overriding plates, in this investigation, we elucidate the tectonic and mechanical processes leading to the M_w7.0 (moment magnitude of 7.0) Acapulco, Mexico, earthquake in 2021. We exploit unprecedented ocean-bottom observations using ultralong-period "tilt mechanical amplifiers," along with hydrostatic pressure, global navigation satellite system, and satellite interferometric synthetic aperture radar data. The joint inversion of these geodetic data, template-matching seismicity, and repeating earthquakes, revealed the first two shallow slow slip events (SSEs) observed in Mexico. The first one migrated from the trench to the earthquake hypocenter before rupture, and the second one occurred following an M_w7.3 long-term SSE induced by the earthquake. Episodic near-trench oceanic-crust deformations (i.e., tilt transients) associated with shallow and deep synchronous decoupling of the plate interface reveal the occurrence of "slab-pull surges" before three regional earthquakes of magnitude 7 or greater, including the Acapulco event, suggesting that they may serve as rupture precursors observable in subduction zones.

INTRODUCTION

Seafloor geodesy in subduction zones has gained remarkable importance in the past decade. Several groups have instrumented the seafloor down to the oceanic trench looking for transient deformations caused by tectonic processes such as slow slip events (SSEs). An emblematic case is the Eastern Japan and Nankai subduction zones, where the world's largest seafloor observatories, S-net and DONET, were deployed in the aftermath of the 2011 Tohoku-Oki megathrust earthquake (*1*). Further efforts have been made in Japan (*2*) and other regions such as the margins of Costa Rica (*3*), New Zealand (*4*), Mexico (*5*), Cascadia (*6*), Alaska (*7*), and Chile (*8*) to gain insight into the plate interface processes that generate large earthquakes and tsunamis.

The evidence of SSEs from seismological analysis is well documented and encompasses a wide range of slow earthquakes, from tectonic tremor to very-low-frequency events. Seismic records have yielded remarkable insights into the strain evolution in the megathrusts, both in the deep and shallow transition zones that flank the locked interface depths (*9*–*16*). The migration and sensitivity of tremor sources are closely linked to overpressured fluids at the interface, which can vary in space and time depending on the amount of water embedded in subducted sediments, the oceanic crust, and the upper mantle (*17*–*21*). The inherent heterogeneity of the plate contact and the irregularity of the interface result in the segmentation of seismic behavior along the megathrusts (*22*–*24*). This is illustrated by the Guerrero subduction zone in south-central Mexico, which is the location of the world's largest SSEs (*25*, *26*) and a major seismic gap that has long been feared (*27*, *28*). Should an earthquake with a magnitude greater than 8 break through the gap, the strong motions in Mexico City could be threefold those registered during the catastrophic 1985 Michoacán earthquake (*29*, *30*), which resulted in the deaths of at least 10,000 people in the country's capital.

The potential for large earthquakes is closely related to the occurrence of SSEs (*2*, *31*–*34*). Continuous monitoring of seafloor crustal deformations and seismicity using frontline observatories is a crucial step in the development of predictive models aimed at identifying potential locations and timing for future devastating earthquakes and tsunamis. The development of Global Positioning System (GPS)–acoustic measurements of seafloor transponder arrays has a long history (*35*, *36*), leading to the advent of high-tech, lower-cost observational protocols using autonomous devices such as wave gliders (*5*, *37*, *38*). Nevertheless, understanding the tectonic processes occurring at timescales that are crucial for comprehending the short-term dynamics that precede major earthquakes remains elusive using these devices. Ocean-bottom pressure (OBP) gauges (also referred to as absolute pressure gauges) are more appropriate instruments and the most easily deployed and commonly used for measuring SSE-induced vertical deformations (*2*, *4*, *6*, *39*). However, in addition to the intrinsic drift they suffer (*40*), these single-component sensors are so sensitive that both tidal and nontidal oceanographic signals often mask tectonic deformation (*6*, *41*–*43*). Long-base tiltmeters onshore (*44*) and borehole tiltmeters offshore (*45*, *46*) suffer from similar problems, where noise could potentially overwhelm these highly sensitive and costly devices.

The present study investigates the seismogenesis of the Guerrero seismic gap (GGap) through an analysis of a comprehensive set of seafloor instruments and observations. These include newly developed low-cost, virtually noise-free ocean-bottom tiltmeters (OBTs)

[1]Instituto de Geofísica, Universidad Nacional Autónoma de México, Mexico City, Mexico. [2]Facultad de Ingeniería, Universidad Nacional Autónoma de México, Mexico City, Mexico. [3]Disaster Prevention Research Institute, Kyoto University, Kyoto, Japan. [4]Instituto de Ingeniería, Universidad Nacional Autónoma de México, Mexico City, Mexico. [5]Department of Civil Engineering, California State University, Los Angeles, CA, USA. [6]Laboratoire de Géologie, École Normale Supérieur de Paris, Paris, France. [7]Institut Terre et Environnement, Université de Strasbourg, Strasbourg, France. [8]Lamont Doherty Earth Observatory, Columbia University, New York, NY, USA. [9]Instituto de Ciencias del Mar y Limnología, Universidad Nacional Autónoma de México, Mexico City, Mexico.
*Corresponding author. Email: cruz@igeofisica.unam.mx

and OBP sensors with continuous records spanning 5.4 years, during which four M7+ (magnitude 7 or greater) regional earthquakes have occurred. These observations are complemented by measurements from a dense global navigation satellite system (GNSS) network and satellite interferometric synthetic aperture radar (InSAR) onshore. One of the tiltmeters was deployed over the incoming Cocos plate, situated only 10 km from the Middle America trench, while the remainder was distributed inside the gap on the overriding North American plate. All instruments, including broadband seismometers on land, recorded tectonic activity both before and after the 2021 M_w7.0 (moment magnitude of 7.0) Acapulco earthquake (*47*, *48*). Collectively, the data offer a distinctive perspective on the seismogenesis of this event and of the other regional earthquakes—a scenario that could potentially shed light on the origin of future major ruptures in the seismic gap and other regions of the globe.

RESULTS

In November 2017, we deployed the first Mexican seismogeodetic amphibious network across the GGap (*5*). In addition to the onshore installation and/or maintenance of 34 GNSS stations and 8 broadband seismometers in the state of Guerrero, 43 ocean-bottom instruments (geodetic and seismic) were periodically installed and maintained for different research purposes, and data were acquired until April 2024. This objective was achieved through eight oceanographic expeditions conducted aboard the R/V El Puma, operated by the National Autonomous University of Mexico (UNAM), in addition to an associated campaign undertaken in 2022 aboard the R/V Marcus G. Langseth, operated by Columbia University.

Except for one (OBO8 installed in March 2022), all other ocean-bottom observatories (OBOs) were installed in November 2017 between ~1000 and 4992 m in depth (Fig. 1). The eight OBOs were equipped with a Digiquartz pressure sensor (OBP) developed by Paroscientific Inc. and a thermometer. Instruments OBO3, OBO4, OBO5, OBO7, and OBO8 correspond to Fetch units manufactured by Sonardyne Inc. and were also equipped with a high-precision dual-axis digital tiltmeter (OBT) incorporated into a microelectromechanical device within the glass sphere, manufactured by Analog Devices Inc. These units had an acoustic transducer/transponder for data transmission and GPS-acoustic measurements using an autonomous sea surface vehicle in two instrument arrays at OBO4 and OBO5 sites (*5*). OBO1 never responded 1 year after its deployment, and OBO3 had a transmission failure, so no data are available from

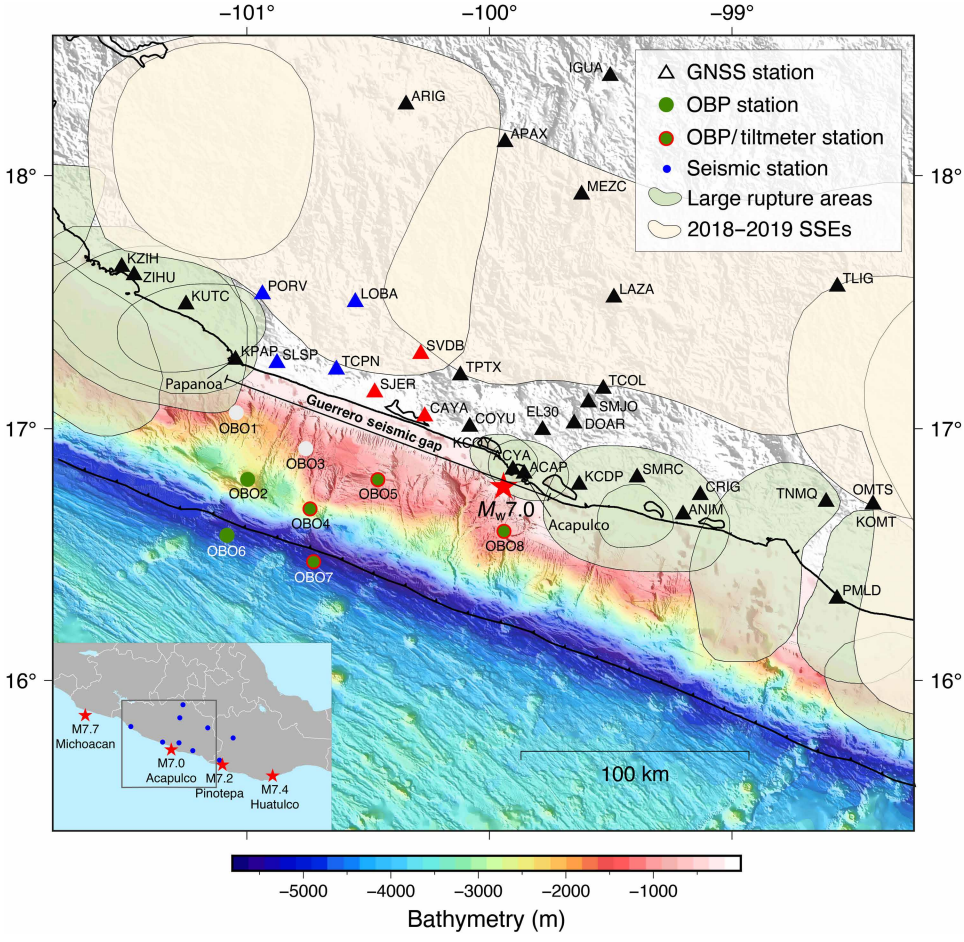

Fig. 1. Geographical location of the geodetic and seismic stations used in this work. In addition, the epicenter of the 8 September 2021 Acapulco earthquake (red star), the high-resolution bathymetry of the GGap determined from subsequent campaigns, the rupture areas of the historical earthquakes, and the most recent SSE of 2018 and 2019 before this research are also shown.

either site. Covering the whole period 2017–2024, the 34 GNSS stations were operational onshore either continuously or partially.

During the 5.4 years of continuous data acquisition, at least two previously documented M7+ SSEs occurred in Guerrero in 2018 and 2019 (*33*), and four M7+ thrust earthquakes happened in south-central Mexico (see Fig. 1 for event locations). Epicentral distances of the earthquakes to the seafloor stations ranged from 490 km for the 2020 M_w7.4 Huatulco earthquake to 55 km for the 2021 M_w7.0 Acapulco earthquake. This provides an exceptional opportunity to study the effects at the plate interface within the GGap caused by prominent regional slow- and fast-slip events.

The M_w7.0 Acapulco earthquake

On 8 September 2021, an M_w7.0 thrust earthquake occurred beneath Acapulco, right in the heart of the GGap (*47*, *48*) (hereinafter "Acapulco earthquake"), with its epicenter 55 km east of station OBO5 (Fig. 1). Without a doubt, this earthquake is the best near-field ever recorded in Mexico both seismically and geodetically. Figure 2 shows the coseismic slip distribution derived from the joint inversion of 15 GNSS displacements, first used here (figs. S1, S2, and S3B), and a saliency-based quad-tree–sampled Sentinel satellite interferogram (fig. S3) (*49*), using the ELADIN (elastostatic adjoint inversion) method (*50*, *51*). The "Acapulco earthquake coseismic

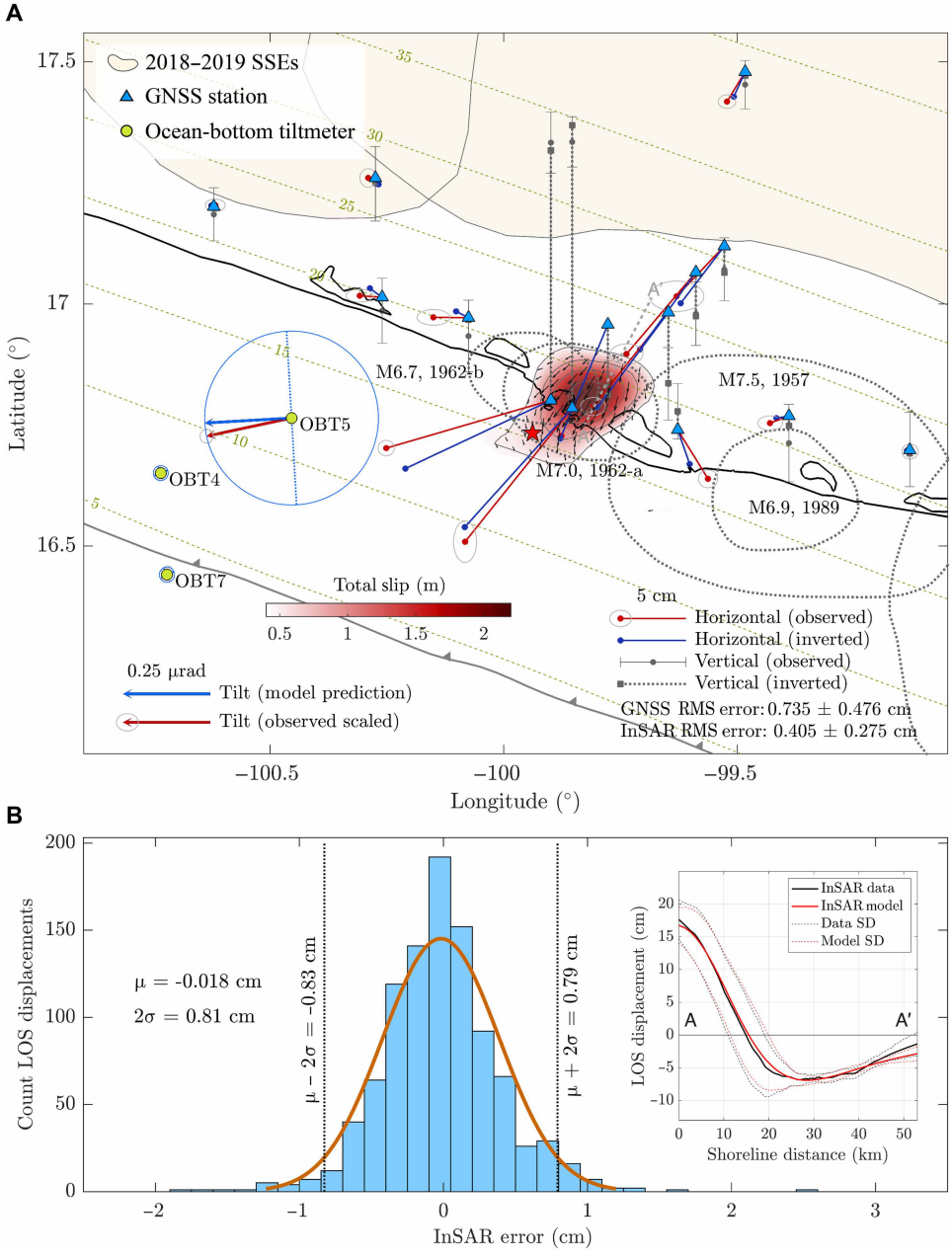

Fig. 2. Joint coseismic inversion of GNSS and InSAR data from the 8 September 2021 earthquake beneath Acapulco (M_w7.0). (**A**) Slip distribution accompanied by fit of displacements at GNSS stations, rupture areas of historical earthquakes, and comparison of model-associated theoretical tilt with observed tilt (scaled) at three OBTs. The blue circles and dotted lines represent the tilt amplitude and tilting axis, respectively. (**B**) Distribution of InSAR errors and average fit of observed line-of-sight (LOS) data along the profile shown in (A) within a vicinity of 10 km around the profile (inset).

slip inversion" section provides details about this inversion. The slip distribution features a main, well-localized asperity with a maximum slip of 2.3 m located within the rupture area of the 11 May 1962 earthquake (see dotted ellipse on Fig. 2A) and confirms a northeast (i.e., downdip) rupture directivity from the hypocenter (*47*), located offshore about 20 km southwest of the asperity. This rupture is a repeat of the M_w7.0 1962 event (*52*) that was followed by a M_w6.7 doublet 9 days later next to the M_s7.5 (surface wave magnitude 7.5) Acapulco–San Marcos rupture of 1957, which toppled the Angel of Independence emblematic monument in the country's capital and gave birth to earthquake engineering in Mexico.

The Guerrero gap is well known for its large SSEs that may propagate to shallow, seismogenic depths between Acapulco (100°W) and Papanoa (101°W) (*25*, *33*, *50*) (Fig. 1). This 130-km-long segment defines the oldest part of the seismic gap, where the last M7+ rupture took place 113 years ago, on 16 December 1911 (M_s7.6) (*28*). Thus, the 2021 Acapulco earthquake occurred where the gap extends southeastward in a 110-km-long segment that hosted the M_s7.5 Acapulco–San Marcos earthquake 67 years ago, on 28 July 1957 (Fig. 2A). It is also known that SSEs can play an important role in the initiation of large ruptures (*2*, *31*–*34*), and the recent record from Mexico shows that the last four M7+ thrust earthquakes preceding the 2021 Acapulco event in the states of Guerrero and Oaxaca were triggered, or at least preceded, by an SSE downdip from and near their hypocenters. These events include the M_w7.5 2012 Ometepec (*53*), the M_w7.3 2014 Papanoa (*34*), the M_w7.2 2018 Pinotepa (*33*), and the M_w7.4 2020 Huatulco (*51*) earthquakes. Whether a similar phenomenon happened in the Acapulco rupture is one of the questions we will explore using unprecedented data.

Transient forearc deformation: Offshore and onshore data

Available hydrostatic pressure records until March 2023 with a sampling rate of 30 min are shown in Fig. 3A along with the timing of the SSEs in Guerrero mentioned earlier and the M7+ thrust earthquakes in south-central Mexico (see Fig. 1 for event locations). An effective way to reduce noise associated with tidal and nontidal oceanographic components is correcting pressure from collocated temperatures, which are often correlated at sites lying on the continental shelf (fig. S7) (*42*). Common noise across the station array associated with long-wavelength signals can also be reduced by subtracting a reference site minimally affected by the tectonic effects under study (*2*, *4*). The "Analysis of OBP data" section provides details of the noise reduction procedure we applied.

Inspection of the temperature-corrected pressure at OBP5 relative to the Cocos plate (Fig. 3B) (i.e., relative to OBP7) reveals that 3 months before the 2021 Acapulco earthquake, the water column began shrinking to about 3 cm at the time of the earthquake. Also remarkable is the permanent deviation of pressure from the drift model during the year and a half following the event. Although uncertain because the linear drift model does not fully capture the data in the regression window, the relative water column at OBP4, the site closest to the trench in the overriding North American plate, may also have decreased by ~1 cm (Fig. 3C). Since (i) pressure evolution at both sites relative to the same reference (OBP7) is substantially different and (ii) the pressure time series at OBP4 and OBP7 are very similar to each other (fig. S7C), then the prominent pressure drop in OBP5 responds to a local phenomenon producing progressive seafloor uplift during the 3 months preceding the earthquake. This is our first evidence pointing to the occurrence of an SSE somewhere

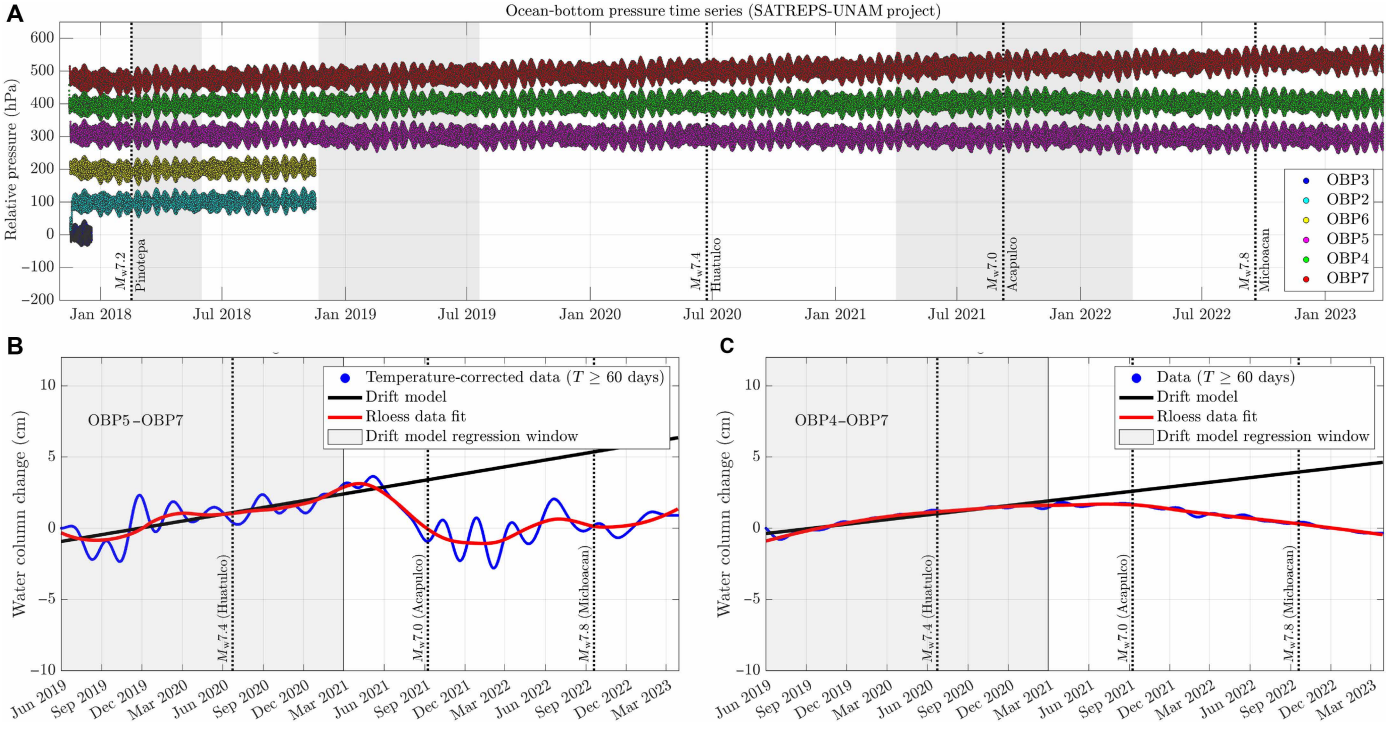

Fig. 3. Continuous hydrostatic pressure records at OBP stations for 5.4 years. (**A**) Raw data along with timing of large regional earthquakes (dotted lines) and duration of deep SSE in the Guerrero gap (gray shaded). SATREPS, Science and Technology Research Partnership for Sustainable Development program in Japan. (**B** and **C**) Temperature-corrected seafloor pressures at OBP5 and OBP4 relative to OBP7 (Cocos plate) in the period surrounding the Acapulco earthquake. The gray shades depict the regression window to fit the drift model (black lines). Rloess refers to locally weighted non-parametric regression fitting using a second-order polynomial.

below the seafloor in that period. OBP5 is about 30 km from the coast; therefore, we analyzed its closest GNSS time series as follows.

Onshore, seasonal noise–reduced displacements (*51*) (fig. S9) at four GNSS sites ~60 km northwest of OBP5 indicate that, during the same 3-month period preceding the earthquake, the coastal subsidence rate characteristic of interseismic periods in Guerrero was prominently increased (blue sites in Figs. 1 and 4A). This can be better appreciated in the detrended mean of the vertical components (Fig. 4B) and possibly related to a slip transient updip in the plate interface (possibly an offshore SSE). Although the mean horizontal displacements along the plate-convergence direction show no substantial rate change before the Acapulco earthquake, they do at the three closest GNSS sites about 30 km north-northeast of OBP5 (red sites; Figs. 1 and 4C). A visual inspection of the north and east components at these sites (Fig. 4A) reveals that this rate change corresponds to a slowdown of the interseismic deformation during the 3 months before the earthquake. At CAYA station, the closest site to OBP5, the vertical displacement rate tends to change its polarity from subsidence to incipient uplift during the same period that OBP5 experienced the uplift referred to above (Figs. 3B and 4A). Selected GNSS displacements in Fig. 4A also show the large postseismic release during the 9 months following the earthquake, which, as we shall see, primarily corresponds to a large, long-term SSE induced by the rupture.

Ocean-bottom ultralong-period tilt mechanical amplifiers

Nonharmonic noise could dominate the bandwidth of interest in OBTs and pressure gauge data. Nontidal oceanographic fluctuations of the water column can seriously obscure the information (*41*–*43*, *45*, *46*). This indicates that the stillness of the deep ocean and the

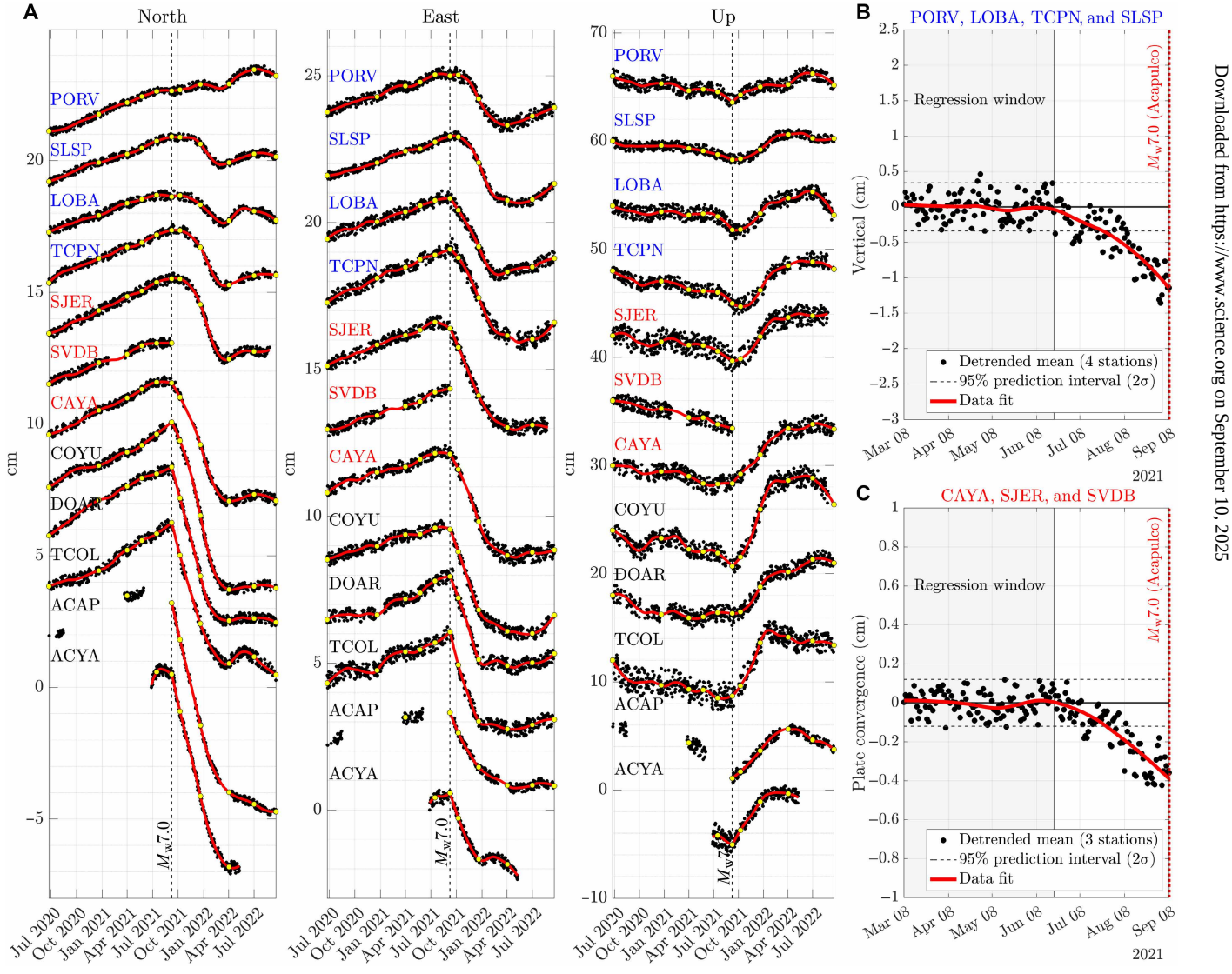

Fig. 4. GNSS displacement time series surrounding the Acapulco earthquake after outlier and seasonal noise reduction. (**A**) Yellow dots indicate the bounding dates of the inverted time windows. Blue and red fonts are associated with (B) and (C), respectively (and color-coded stations in Fig. 1). (**B**) Average detrended vertical displacements at sites marked with blue fonts. (**C**) Average detrended displacements parallel to the plate convergence direction at sites marked with red fonts. The gray shades in (B) and (C) depict the regression windows used for detrending the signals.

extreme sensitivity of some geophysical instruments do not necessarily facilitate the detection of tectonic deformation. An alternative to alleviate this problem might come from noise-insensitive devices that amplify potentially useful signals over a known bandwidth. As demonstrated below, low-cost tiltmeters housed within a glass sphere mounted on a steel tripod over highly compressible marine sediments act as ultralong-period tilt mechanical amplifiers (TMAs) that detect slow tectonic deformations and are blind to most oceanographic noise.

Ocean-bottom Fetch units OBO4, OBO5, OBO7, and OBO8 (Fig. 1) are equipped with two-component high-precision tiltmeters within a glass sphere that are mainly designed for unit control. According to the manufacturer, the sensitivity of these sensors is 436 μrad, so, at first sight, they should be blind to expected secular or transient tectonic deformations on the order of units of microradians per year (*44*, *45*). As a proof of concept to assess whether the TMAs could detect tectonic deformations, we will develop a simplified, two-dimensional model under conditions close to those expected in our ocean-bottom instruments.

Neglecting any possible oceanographic effects, the instrument tilt depends on (i) the tectonic tilt (i.e., the hard-rock basement tilt) and (ii) the response of the highly compressible fluid-saturated seafloor sediments to the differential forces applied by the instrument legs as the basement tilts (Fig. 5A). The problem thus reduces to estimating these forces for a given basement tilt and then quantifying the differential settlements of the sediments surrounding each leg. With these elements, the effective instrument tilt can be estimated and compared to the basement tilt. The detailed model description to address this problem in found in the "TMA model" section.

From our model, we can thus distinguish between α, the slow tectonic (basement) tilt, and α_s, the settlement-induced tilt due to the differential settlements underneath the unit legs (because $\delta_1 > \delta_2$; Fig. 5A). The effective (or total) instrument tilt, which is the observable measured by the tiltmeter within the glass sphere, is then given by $\alpha_{tot} = \alpha + \alpha_s$, and we define $A_t = \alpha_{tot} / \alpha$ as the tilt amplification factor that we expect to be larger than one.

Figure 5B shows the evolution of α_{tot} as α increases linearly from 0 to 2.5 μrad. The simulation results are shown in terms of the settlement at the surface (left axis) and A_t (right axis), both as a function of α, for the indicated typical values of the sediment compressibility index (C_c), void ratio (e_0), and effective stress gradient (γ). The blue and orange dots correspond to the values of each function when α_{tot} exceeds the tiltmeter sensitivity threshold of 436 μrad. At that moment, sediments under leg 1 have settled 0.48 mm, and α has been amplified 402.5 times. It is also clear that settlement and, thus, tilt amplification grow exponentially with α. However, we will see later

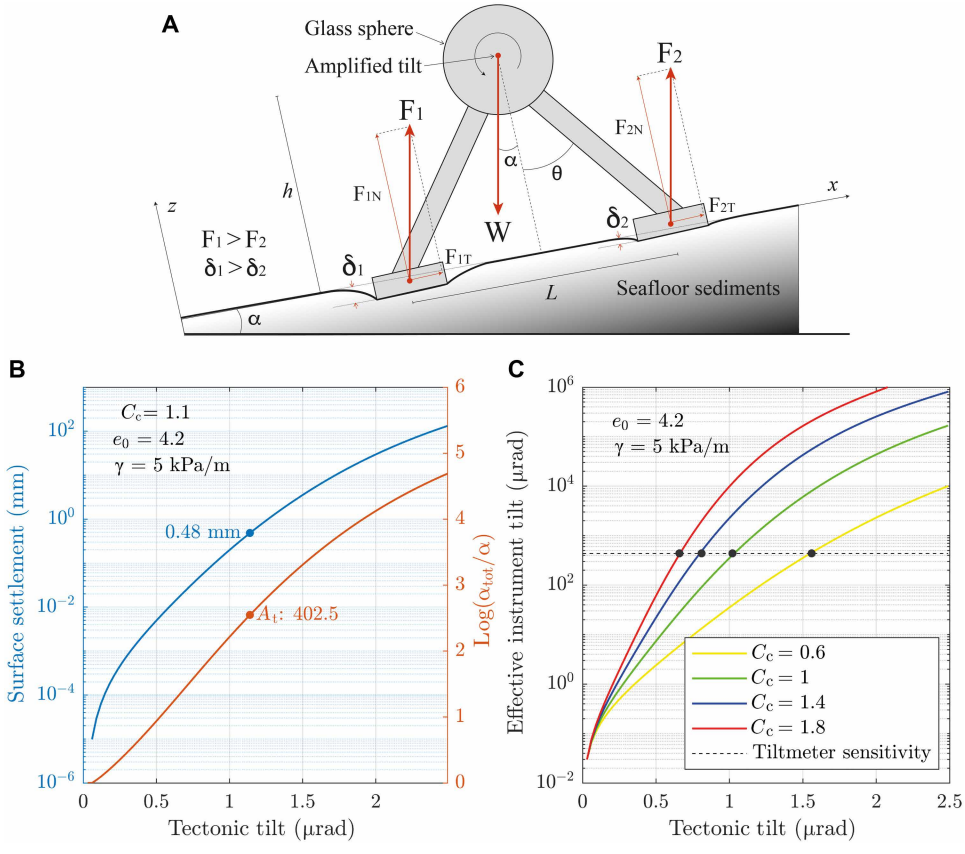

Fig. 5. Performance of an ultralong-period TMA. (**A**) Simplified body diagram of a Fetch unit upon highly compressible seafloor sediments after a basement tilt α. (**B**) Sediment settlement (left axis) and tilt amplification (right axis) as a function of basement tilt incorporating the highly nonlinear sediments response to the differential Fetch unit leg forces. Dots indicate when tilt amplification reaches the instrument sensitivity threshold for the given sediment properties, where C_c stands for the compressibility index, e_0 for the void ratio, and g for the effective stress gradient. (**C**) Effective instrument tilt within the glass sphere as a function of basement tilt for different sediment compressibility values (C_c).

that since the expected transient change of the actual tectonic tilt is within ~0.5 μrad, the variation of the amplification factor in that range should not exceed one order of magnitude. Figure 5C and fig. S11C show the evolution of α_{tot} and δ as the basement tilts, respectively, for a wide range of compressibility indexes covering most of the values determined for marine sediments (*54*, *55*), as illustrated in fig. S11D. The black dots indicate again the moments when α_{tot} overcomes the tiltmeter sensitivity threshold. Given the chosen values for e_0 and γ, the instrument threshold is reached in all instances for tectonic tilts smaller than about 1.5 μrad. The black curve of fig. S11D depicts the α values reaching the instrument sensitivity as a function of C_c for the chosen conservative parameters and a compressibility range for different types of marine sediments after Davie *et al.* (*54*) and Hampton (*55*).

On the basis of this analysis, we conclude that Fetch units act as seafloor TMAs that can measure basement tilts within the expected range for tectonic plate interaction–induced deformations. Different values for e_0 and γ were also explored with even more favorable results, for example, when considering smaller void ratios observed in marine environments, which can be as small as 1.6, or considering lower stress gradients up to 2.5 kPa/m that have also been measured in seabed clays. It should therefore be noted that uncertainties in the properties of the sediments mean that the model developed here should only serve to provide confidence in the interpretation of the tilting data presented next.

SSE-induced seafloor tilt

Available tilt raw data from stations OBT4, OBT5, OBT7, and OBT8 with 24-hour sampling rate are shown in the left column of fig. S12. Among the discontinuities found, the most prominent in both components is from the M_w7.0 Acapulco earthquake at station OBT5 (Fig. 1 and fig. S12). To estimate the orientation of the tiltmeters, we used baselines from the outlier-free time series shown in the right column of fig. S12. The procedures for both this estimation and outlier removal are described in the "Tilt data analysis" section. If the hypothesis underlying the orientation of the tilt sensors is correct, i.e., that the baselines tilt rates are dominated by the long-term interplate interaction, then we would expect the tilt discontinuity observed in OBT5 from the 2021 Acapulco earthquake to be close to the theoretically expected direction. Figure 2A shows the comparison of this observed discontinuity with the coseismic tilt predicted by Okada's model (*56*) associated with our coseismic slip distribution. This calculation considers the site bathymetric elevation. The dotted line in the tilt representation depicts the basement tilt axis, and the arrow depicts the theoretical tilt vector. Although the magnitude of the observed discontinuity has been normalized to the theoretical value, the consistency in the direction of both quantities is remarkable and gives confidence in both the TMA model and the procedure introduced for the orientation of sensors.

To remove the sediment-induced tilt amplification from the data, following Cruz-Atienza *et al.* (*33*), we first inverted GNSS data for the inter-SSE deformation period between 1 September 2019 and 1 April 2021 (Fig. 4) to retrieve the plate interface coupling, defined as $1 - v / v_{pl}$, where v is the interplate slip rate, v_{pl} is the plate convergence rate equal to 6.6 cm/year in Acapulco (*57*), and $v \leq v_{pl}$. For this purpose, we used the same ELADIN method (*50*) as for the coseismic slip inversion, which honors physically consistent restrictions at the plate interface (i.e., slip rake angle, tectonically admissible backslip, and von Karman slip distributions) via a gradient projection strategy (*33*, *51*). Details of the inversion and resolution analysis can be found in the "Inter-SSE plate interface coupling inversion" section. The benefit of using offshore data including tilt in the inversions will be discussed in the "Joint inversion of seafloor tilt, hydrostatic pressure, and GNSS data" section and can be appreciated in fig. S17 for a checkerboard inversion test.

Figure 6 presents the inter-SSE coupling inversion of three-component GNSS data along with the aftershock areas of all historical earthquakes in the region (brown shapes). Although we believe that our long-standing pressure records are devoid of substantial instrumental drift and thus useful for the inversion, we did not include in the inversion the secular vertical displacements at OBP4 and OBP5 referred to the Cocos plate (i.e., to OBP7) (Fig. 3, B and C). However, when comparing these displacements with the theoretical prediction derived from the coupling model (blue vertical bars), we find that they are consistent, which points to the validity of our drift conjecture.

As previously found by Radiguet *et al.* (*25*) during short-term inter-SSE deformation periods, the interface coupling between Papanoa (101°W) and Acapulco (100°W), i.e., within the oldest segment of the seismic gap, is substantially deeper (about 10 to 15 km) and greater (reaching values of 0.8) than in the adjacent segments. For instance, the 0.4 coupling contour (red dashed lines) is deflected into deeper regions along the gap and encloses the shallower rupture zones of earlier earthquakes. Also interesting is the offshore rapid decrease in coupling when approaching the trench in the gap, with values below 0.1 for depths smaller than 10 km (i.e., along a ~25-km-wide and ~150-km-long trench-parallel interface strip). Although this coupling pattern suggests a very particular mechanical behavior of the interface that could partially explain the existence of the seismic gap, we note that it does not reflect the effective long-term stressing rate since deep SSEs periodically occur in Guerrero, releasing a large part of the accumulated strain energy where coupling is the largest, around 35 km in depth (*25*).

From our inter-SSE coupling inversion, we can calculate the theoretical tilt rates at the tiltmeter locations using Okada's model (*56*) to compare with the observed rates determined from the baselines used to orient the sensors, reported in table S2. Figure 6 shows those model predictions (green arrows), with magnitudes of 0.245 μrad/year at OBT4 about 9 km from the trench, 0.427 μrad/year at OBT5, and 0.406 μrad/year at OBT8, both sites about 30 km from the trench. The estimated long-term rate of −0.5 μrad/year on the Cocos plate (i.e., at OBT7, which sits on the footwall) was derived independently from the geometry of the Cocos plate and its no-net rotation motion (*58*). On the basis of the global multiresolution ocean elevations data (*59*) (i.e., bathymetric data), the convex geometry of the Cocos plate in the vicinity of the trench was described by fitting a polynomial (no matter whether second or third degree), so that, by multiplying the spatial derivative of this function at the OBT7 location by the plate velocity, the secular tilt rate was estimated. Note that tilt rates away from the trench (in OBT5 and OBT8; Fig. 6) are about 15% smaller than in the Cocos plate and twice as high as predicted near the trench in the overriding plate (OBT4). From these theoretical tilt magnitudes and those determined from the data baselines, we can estimate the tilt amplification factors, A_t, at each site as reported in table S2, which range from 849 on the Cocos plate to 5757 on the overriding North American plate. The much higher amplification at OBT8 is certainly related to two factors: a much higher tilting rate in the baseline due to the ongoing

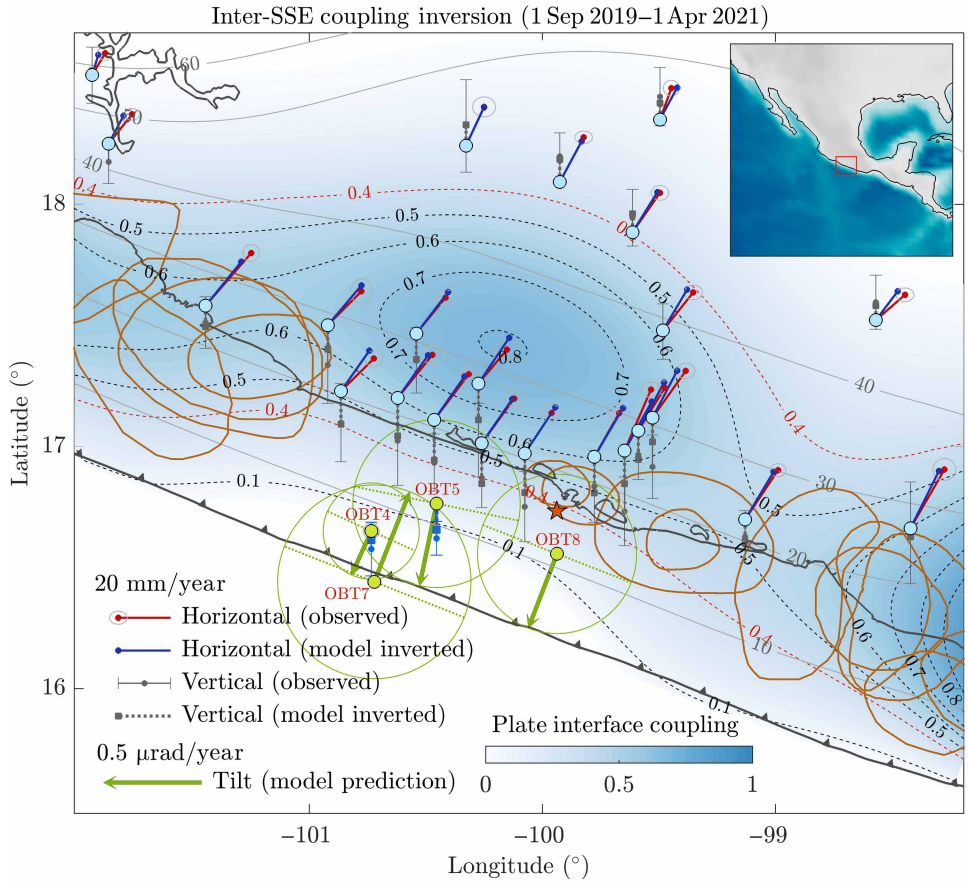

Fig. 6. Inter-SSE plate interface coupling inversion from GNSS displacements. Tilt model predictions at our forearc seafloor tiltmeters OBT4, OBT5, and OBT8 are shown with green arrows, where the green dotted lines indicate the tilting axis. Tilt at OBT7 upon the Cocos plate was estimated independently (see text). Predictions for the vertical displacement at OBO4 and OBO5 are compared with drift models shown in Fig. 3 (B and C). Brown shapes delineate historical rupture areas.

SSEs throughout the recording period and the sediment properties in the continental slope down from Acapulco Bay, where several submarine canyons surround the station (unlike OBT5; Fig. 1) and, thus, where sediment compressibility may be higher than 1.8 (*54*). On the other hand, since OBT4 is characterized by a steady, secular deformation with no clear trend, we assumed the same amplification for this site as for OBT5, which led to very consistent results, as discussed later.

To correct the tilt data from the sediment-induced amplification, we simply divided the time series by the corresponding amplification factor A_t (table S2). This procedure neglects possible amplification variations predicted by our TMA model (Fig. 5B). However, this assumption is a reasonable proxy since tectonic tilt changes are within fractions of microradians. Figure 7A displays the amplification-corrected tilt data in the four sites. Because the corrections are based on theoretical predictions, the reported long-term tilt rates should only be taken as self-consistent approximations of the actual plate deformation, useful for the joint interpretation of onshore and offshore data. As we will see, the most valuable information relies on the short-term tilt variations, which often correlate in time between the stations (Fig. 7B, red curves). The wind rose diagrams of Fig. 7A show the tilt rate histograms for 30-day moving windows with 5-day overlap, except for OBP8 where we took 15-day windows. Arrows within the histograms indicate the plate convergence direction, which allows us to see how the tilt directions vary throughout the whole data window compared to that reference direction. For instance, while station OBT7 on the incoming Cocos plate always tilts in the plate convergence direction (northeast quadrant), station OBT5, which is seated on the overriding North American plate, does in the opposite direction (southwest quadrant) except for some tilt reversals that correspond, as we will see later, to transient rebounds associated with SSEs within the blue and red background shades (Fig. 7B). On the other hand, station OBT4, which is close to the trench upon the forearc, features a much steadier behavior with tilt episodes covering all azimuths. The most rapid tilting period occurred at OBT4 during the 2018 Guerrero SSE just after the Pinotepa earthquake (*33*).

Figure 7B shows an onshore-offshore multiple data comparison. For better inspection, all time series were detrended using linear regressions between the yellow dots covering a 6-month quiescent period, and GNSS coseismic discontinuities were removed. Positive tilt increments will from now on represent seaward tilt opposite to the Cocos plate convergence, while negative increments will represent tilt in the Cocos plate convergence direction. The two selected GNSS time series (green curves) essentially show the 2019 and 2021 deep SSE in Guerrero (blue shades), with some variability around them. With a clear delay compared to the GNSS signals, transient tilt variations are also present in the three tiltmeters for the 2019 and 2021

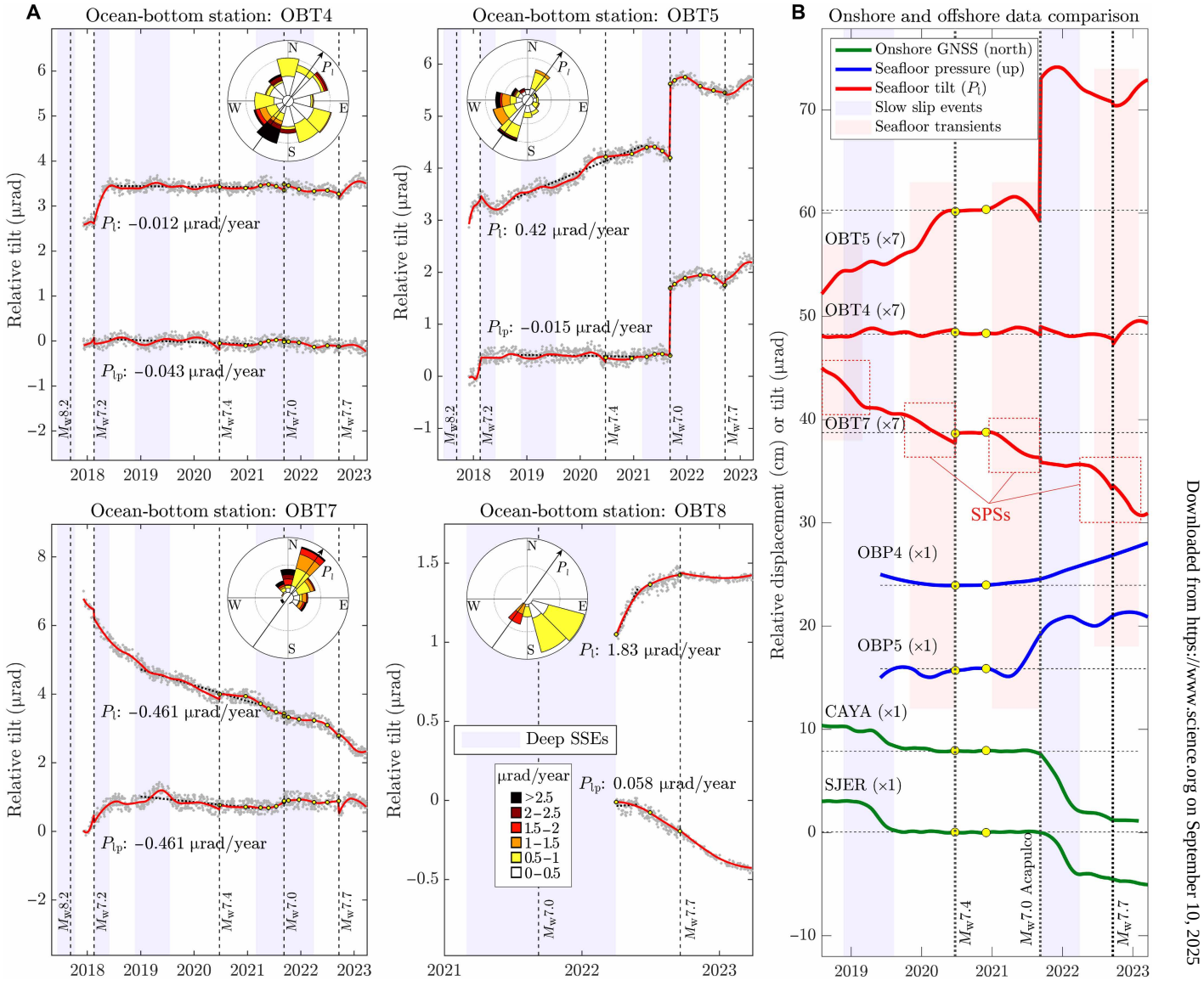

Fig. 7. Observed seafloor tilt and comparison with independent data. (**A**) Tilt data along the plate convergence (P_l) and its perpendicular (P_{lp}) directions at our four tiltmeters after sensors orientation and calibration from theoretical predictions during an inter-SSE period. The wind rose histograms indicate tilting directions and rates from 30 days moving windows with 5 days overlap, where the arrows indicate the plate convergence direction. Reported tilting rates detach from the linear regressions shown as black dotted lines. Yellow dots indicate the boundary dates of the 10 inverted time windows. (**B**) Comparison of tilt data in the long-standing stations (red) with collocated vertical displacements at OBP4 and OBP5 (blue; Fig. 3, B and C) and two selected GNSS sites near the coast (green; see Fig. 1). All data were detrended from linear regressions between the yellow dots for comparison. The red dotted rectangles indicate the occurrence of slab-pull surges (SPSs).

SSEs. Nonetheless, the seafloor data further feature very rich, potentially meaningful transients absent or barely present at the onshore sites (red shades). To assess whether these data fluctuations correspond to tectonic deformations, consistency between different sites and types of data is important. For instance, within the red shade preceding the Acapulco earthquake, the three tiltmeters and the two pressure sensors detected relevant to large variations. As discussed in the "Transient forearc deformation: Offshore and onshore data" section, during that period, only the stack of GNSS data allowed us to see the onshore elastic rebound before the earthquake (Fig. 4B).

A noteworthy and meaningful observation emerges when the tilt history at OBT5 is compared with that at OBT7 on the Cocos plate (Fig. 7B). With the exception of the postseismic period following the Acapulco earthquake, which may be regarded as exceptional in terms of the dynamic and mechanical consequences associated with the rupture, there is a consistent pattern. This is when the Cocos plate accelerates tilting; OBT5 also experiences tilt acceleration toward the trench (positive slopes) before stabilizing or reversing sign—for example, if an offshore SSE occurs, as discussed later in the "Near-trench deformations and deep slab activation" section. This can be observed in Fig. 7B during the first three seafloor transients and the latter part of the fourth (red shade).

This multiple-data correlation further suggests that tilt fluctuations actually correspond to offshore tilt due to tectonic activity preceding

the Acapulco earthquake and point toward the same conclusion for other transients such as those depicted by the other red shades around the M_w7.4 Huatulco and M_w7.7 Michoacán earthquakes. Another way to assess whether tilt variations are of tectonic origin is to confront the offshore and onshore data together with a physically consistent plate interface slip model, as discussed in the next section.

Joint inversion of seafloor tilt, hydrostatic pressure, and GNSS data

Because tilt depends on the spatial derivatives of vertical displacement, tilt records are much more sensitive to changes in slip than GNSS and OBP data. Unlike the classical linear inversion of displacement, the joint inversion of displacement and tilt is an optimization problem that requires careful treatment. One way to address this challenge is through regularization of the model parameters. We use the ELADIN method for this inversion because it provides a robust regularization that excludes unrealistic solutions while taking advantage of the tilt sensitivity to slip. Important considerations for properly performing the joint inversion and resolution analysis are detailed in the "Tilt and displacement joint inversion" section.

Figure 8 presents the resulting plate-interface slip at nine different moments along with the observed ocean-bottom tilt (movie S1). Because of the Okada model limitations used to calculate the Somigliana Green's functions (involved in the inversion technique), tilt at OBT7 (Cocos plate) was not used for the inversions but appears in the figure (and movie) for a better and comprehensive assessment of the phenomenology. Figure 8 (A to D) zooms in on the offshore interface activity before the Acapulco earthquake, where a transient SSE initiated in early 2021 next to the oceanic trench (i.e., next to OBO4) and migrated during the following 5 to 6 months toward the coast and then east, toward the earthquake hypocenter in its late stage (also see fig. S18E). The tilt is consistent at OBT4 and OBT5, where it gradually and synchronously changes orientation from southwest to northeast following this slip migration

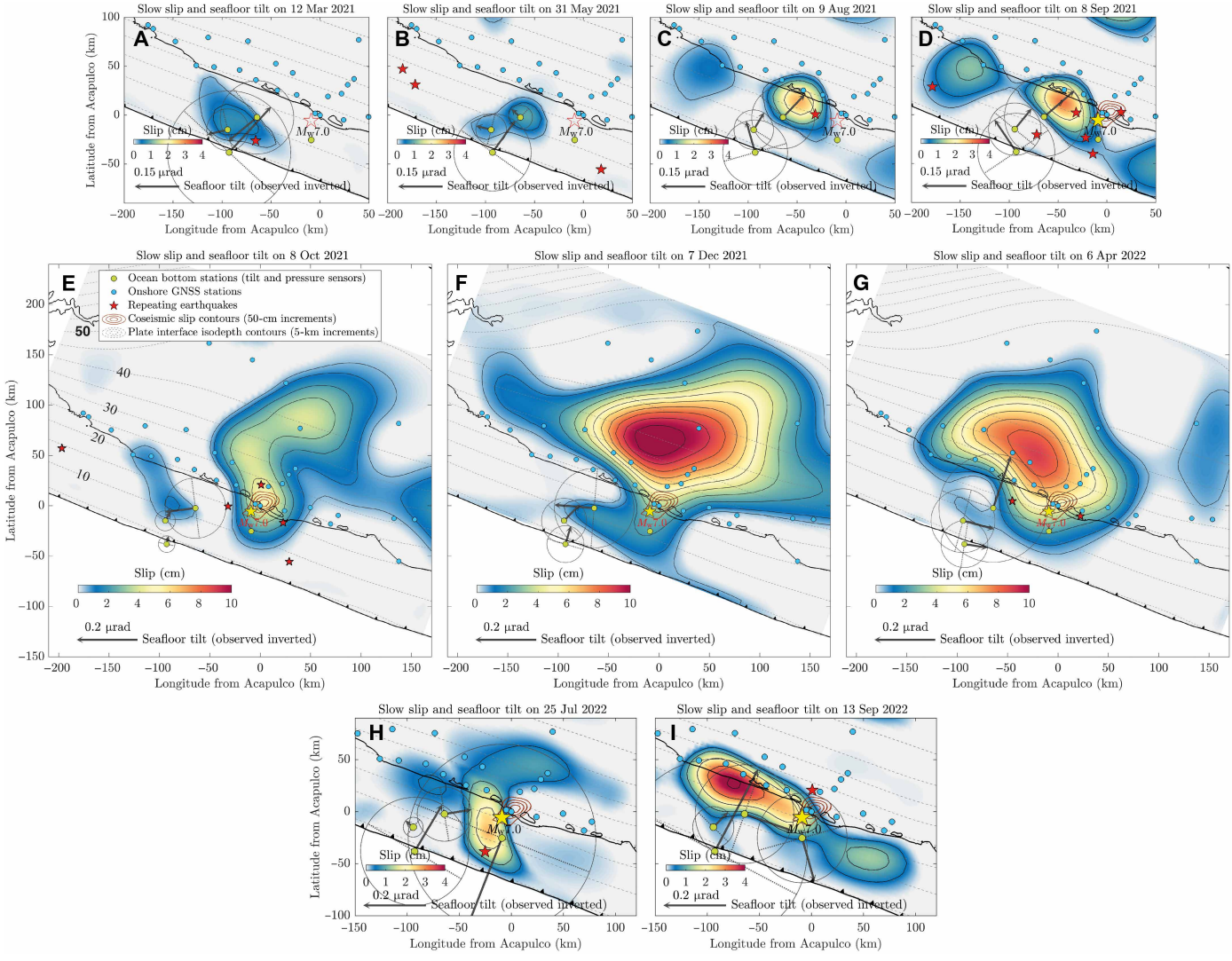

Fig. 8. Plate interface slip evolution from joint inversion of onshore GNSS data and seafloor pressure and tilt data. (**A** to **I**) The slip at the time indicated in each panel heading comes from the interpolation of the 10 inverted solutions whose data fit is shown in fig. S18 (left column). Observed tilt is displayed on each panel (black arrows). The yellow star indicates the Acapulco earthquake epicenter, while red stars the location of repeating earthquakes within ±10 days.

(Fig. 7, A to D, and movie S1). Of substantive importance to validate this result is the consistent vertical deformation recorded in the collocated OBPs, which are also well explained by the model (fig. S18, B to E, left column). An independent (noninverted) and meaningful observation comes out from OBT7 on the Cocos plate, where tilt accelerates when the near-trench SSE develops (Fig. 8A and movie S1). This can be seen in Fig. 7B at OBT7 during the third seafloor transient (red shade), where the Cocos plate undergoes an evolving shoreward tilt of approximately −0.5 μrad from early 2021 that stabilizes about 2 months before the earthquake. To the best of our knowledge, these transient seafloor tilt signals associated with an SSE and the associated inversions are the first to be formally reported.

To assess how much the seafloor data contribute to the inverted models as compared with the onshore GNSS displacements, we performed all the inversions independently (fig. S19) for GNSS data only, for GNSS and OBP data only, and for GNSS and tilt data only. All three inversions determine that an offshore SSE happened along the Costa Grande west of Acapulco during the ~2 months preceding the earthquake (see Fig. 4B and fig. S19E for the GNSS evidence of the SSE). All solutions find also a deep, onshore SSE activated in that period. However, only inversions including data from OBO4 and OBO5 can trace what occurred before and far from the coast. Noteworthy is the occurrence of the aforementioned near-trench SSE during the first 3 months of 2021 and then its slow coastward migration, determined using independent pressure and tilt data. During the ~2 months before the Acapulco earthquake, it is the outstanding tilt transient at OBT5 (see Fig. 7B), which points toward the northeast, that "pushes" the slip eastward toward the rupture hypocenter. Something similar happened during the last two inverted windows (from April to September 2022), when a second offshore SSE took place south and northwest of Acapulco (Fig. 8, H and I, and fig. S19, I and J). As for the remaining windows after the earthquake, when the rupture afterslip and a large long-term SSE occurred, the joint inversions of the whole dataset (Fig. 8, E to G) did not differ substantially from the independent inversions (compare with fig. S19, F to H). All these results show that ocean-bottom tilt and pressure were essential, reliable, and complementary for imaging the evolution of the first two offshore SSEs ever seen in the Mexican subduction zone.

Seismic evidence of slow slip and earthquake nucleation

Slow earthquakes such as tremor and low-frequency events are modulated by slow slip on the plate interface (*15*, *60*), as are repeating earthquakes and background seismicity in general (*61*, *62*). To validate our geodetic inversions and have insights into the plate interface mechanism leading to the M_w7.0 Acapulco earthquake, we develop an independent analysis based on the detection of small, unreported earthquakes by means of a template-matching (TM) technique (*63*) (see the "Template matching analysis" section). We used 3-year-long continuous records from 1 January 2020 to 31 December 2022 at eight broadband seismic stations distributed across the state of Guerrero (inset in Fig. 1) in a region about 480 km in length including the seismic gap (fig. S20A). Our final catalog includes 38,501 events with magnitude larger than 3.2, which is above the completeness value $M_c = 3.1$ (fig. S20, B and C). During this period, 410 of 768 known sequences of repeating earthquakes in southcentral Mexico (*64*) were activated. Representative waveform examples of detected and repeating earthquakes are shown in figs. S21 and S22, respectively.

We seek to identify regions around the plate boundary where seismicity rate anomalies are substantial to assess whether they correlate with the slow slip history determined in the previous section. Furthermore, we are interested in determining whether repeating earthquakes occurred in areas where slow slip was detected by ocean-bottom instruments, which would represent a strong confirmation of the existence of aseismic slip in the surrounding fault matrix (*61*, *62*, *65*). To do so, we first established a baseline for the background seismicity rate between 1 January 2020 and 1 April 2021, a period before the geodetically identified tectonic activity (see the "Background seismicity baseline" section).

The first interesting observation occurs 10 days before the Acapulco earthquake in the two east-west flanks bounding the preseismic SSE offshore, where the seismicity rate increased substantially (Fig. 9A, left). Of particular interest is the seeming increase in the hypocentral region of the Acapulco earthquake, to the east. A detailed analysis of that region, i.e., within 20 km of the hypocenter (Fig. 9B, left), reveals that the seismicity increased well above the baseline during the 15 days before rupture (i.e., the seismicity rate doubled as compared with the five preceding months; right axis), when the offshore SSE pervaded the hypocentral zone (Fig. 8D). During the 3.5 months following the earthquake when the deep long-term SSE starts developing, average deviations largely exceed 50% in two well-localized spots (Fig. 9A, right), with the western patch being larger around the coseismic slip but with a clear offset to the east containing most of aftershocks. The eastern active zone is well defined and away from the seismic rupture (about 60 km), where the M7.5 and M6.9 earthquakes of 1957 and 1989, respectively, occurred. A simple inspection of the seismicity rate history at that spot (movie S2) reveals that during the first 20 days after the Acapulco earthquake, the seismicity sharply increased, suggesting the possibility of an M7+ doublet similar to the 1962 earthquake (Fig. 2A) but this time to the east of the first earthquake.

The occurrence of repeating earthquakes during the preseismic offshore SSE is remarkable. Figure 9B (right) shows these events during the entire geodetically analyzed period along with the cumulative slip (contours) up to the Acapulco earthquake time. Between December 2020 and 8 September 2021, seven repeating sequences activated offshore (inset Fig. 9B, left). The first two sequences, A and B, are very close to the trench (Fig. 9B, right), where the SSE initiated (Fig. 8A and movie S1), while the later four are concentrated where the SSE gained strength, about 15 km offshore (one example is sequence C). Waveforms of the three selected sequences are shown in fig. S22. This evidence is particularly important because it points in the same direction as the seafloor geodetic observations, where a slow dislocation initiated near the trench and migrated slowly toward the coast, where the earthquake occurred. During the first 3 months following the earthquake, the repeaters rate increased sharply (inset in Fig. 9B, left) around the coseismic slip and notably southwest of the hypocenter, where the preseismic SSE pervaded the hypocentral zone. These repeaters span the postseismic slip region (Fig. 8, E and F), both updip and east from the rupture, which provides further confidence about the migration of the SSE southwest from Acapulco, where the preseismic repeaters took place.

Last, we aim to investigate whether slow slip in the hypocentral region was the dominant process leading to the rupture of the M_w7.0 mainshock. We search for evidence allowing us to identify such a process at the plate interface that led to the abrupt increase in foreshocks around the hypocenter (Fig. 9B, left) and, thus, to the

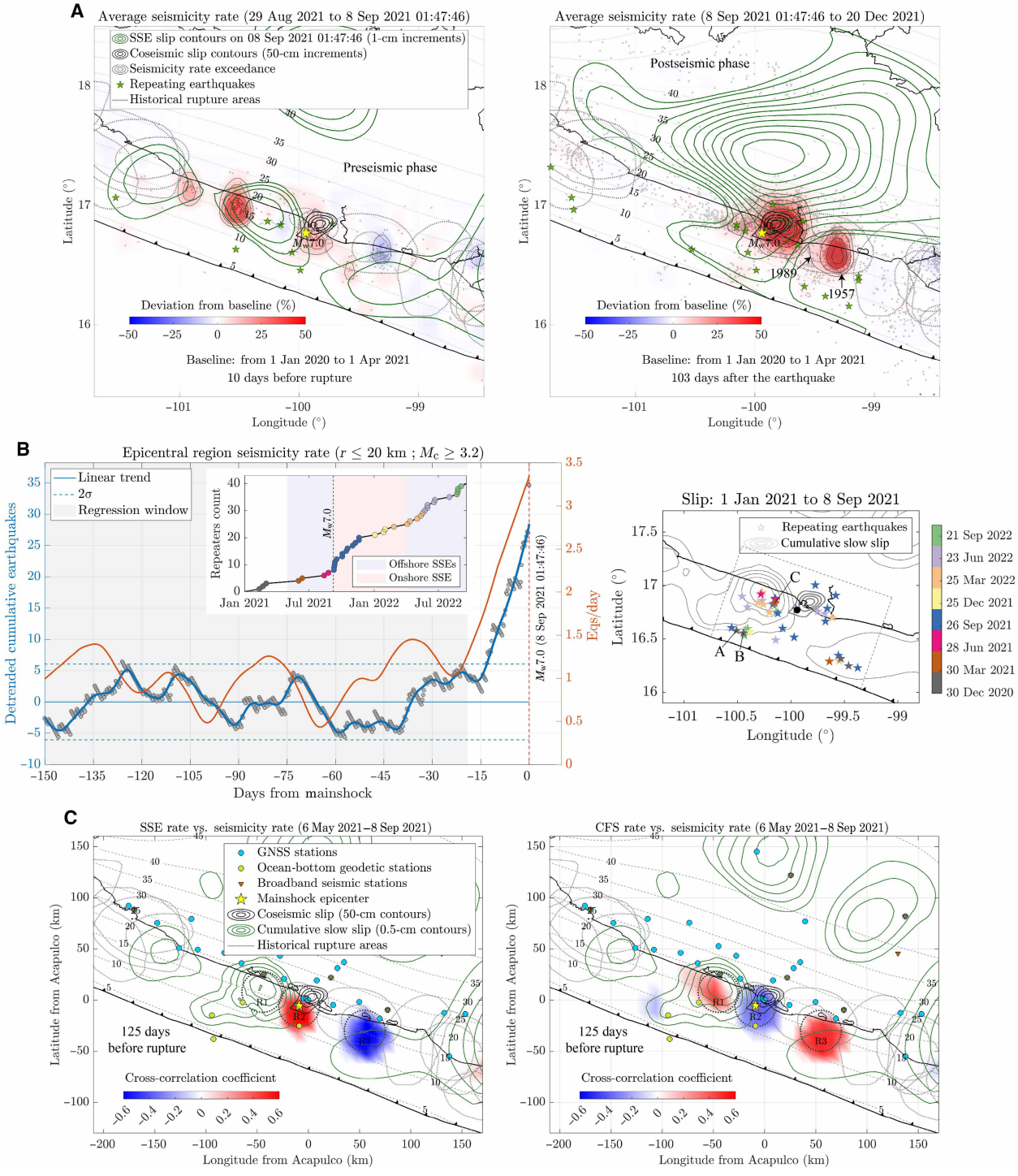

Fig. 9. Analysis of TM seismic detections ($M > 3.2$). (**A**) Seismicity rate deviations from a baseline averaged over the 10 days before the Acapulco earthquake (left) and the 103 days after the rupture (right). Green contours depict the cumulative slip on those periods, and the green stars depict the epicenters of the associated repeating earthquakes. (**B**) Detrended cumulative earthquakes within 20 km from the Acapulco earthquake hypocenter (left axis) and associated occurrence rate (right axis). The inset shows the cumulative repeating earthquakes color coded as identified in the right panel, which shows the events location together with the cumulative slip over the 8 months before the earthquake (contours). Labels A to C indicate three selected sequences whose waveforms are shown in fig. S21. (**C**) Temporal cross-correlation coefficients between seismicity rate deviations and slip rate on the left and CFS on the right, during the 3 months preceding the rupture (see headings). The contours correspond to the cumulative slip during this period.

earthquake nucleation. For this, we calculated the cumulative Coulomb failure stress (CFS) at the interface associated with each geodetic inversion of slip and coupling (fig. S18, right column) using an artifact-free triangular dislocation model (*66*) (see the "CFS and seismicity rate" section).

The most notable evidence appears 3 months before the Acapulco earthquake in the hypocentral region R2 (see Fig. 9C for circular regions location and fig. S24C), where seismicity has a maximum correlation ($cc \approx 1.0$) with slip rate (Fig. 9C, left) and a maximum anticorrelation ($cc \approx -1.0$) with CFS rate (Fig. 9C, right). In contrast, the correlations are roughly reversed during the same period and beyond in the R1 and R3 regions (fig. S24, B and D), where seismicity is highly correlated with the CFS rather than the slip rate. The same result is summarized in the maps of Fig. 9C, which show average *cc* in the 3 months before the earthquake for the slip rate (Fig. 9C, left) and the CFS rate (Fig. 9C, right). Although earthquake nucleation is sensitive to several mechanical and dynamic processes, in this case, the available evidence suggests that it was the slow slip invasion of the hypocentral zone that dominated the foreshock activity and, therefore, likely driven the Acapulco earthquake nucleation over the Coulomb stresses during rupture preparation. Although less representative of short-term interface dynamics due to averaging over a much larger window (see panel headings), the maps in fig. S24A show that slip rate dominated the seismicity rate around the rupture zone and in a wide region east of it, while CFS played its part in the surrounding region, including shallow offshore depths near the trench.

It should be noted that the CFS estimates suffer from notable uncertainties due to the unknown prestress and local mechanical conditions of the interface, so that their predictive power in the short term may be limited. It is also clear from the seismicity rate history (movie S2) that substantial bursts of seismicity alone are not necessarily precursors to a main shock, as shown in Fig. 9A (left), where the most prominent burst occurred west of the Acapulco earthquake hypocenter. Instead, it appears that consistency between seismicity and slow slip may, in some cases, be more predictive of a large rupture, as suggested in Fig. 9C (left).

DISCUSSION

Slip evolution, interface mechanics, and seismogenesis in the gap

During 1.7 years, between December 2020 and September 2022, the plate interface around the GGap slipped continuously with alternating activation depths. In early 2021, an interface dislocation (on the order of 1.5 cm) starts very close to the trench and slowly migrates (during 5 to 6 months) toward the coast where it gains strength from June to develop between 10 and 25 km in depth (M_w6.8 up to 4 cm; Figs. 8, A to C, and 10A). In its final 2-month stage, the event extends eastward to penetrate the hypocentral zone of the M_w7.0 earthquake that occurred on 8 September 2021 (Fig. 8D). Simultaneously starting in July, another slow dislocation initiates at depth (Fig. 10B, fig. S18E, and movie S1). That is, the plate interface decouples simultaneously above 25 km and below 40 km, segments that seem to bound the two transition zones of the interface within the gap where short-term SSEs take place. The shallow SSE is accompanied by repeating earthquakes (from the trench to the shoreline) that corroborate its existence where ocean-bottom geodetic observations (i.e., hydrostatic pressure and tilt) detect it (Fig. 9B). The correlation between the sharp increase in seismicity and slip rate in the hypocentral zone during the 15 days before the mainshock, on the one hand, and the anticorrelation of this seismicity with the CFS (Fig. 9C) suggest that both foreshock activity and earthquake nucleation were dominated by local stress concentration in isolated asperities with aseismic slip surrounding them (Fig. 10B).

Although the juxtaposition of different driving mechanisms certainly results in the nucleation of mainshocks (*62*), the evidence for the Acapulco earthquake suggests that the sharp increase in the foreshock rate around the hypocenter (Fig. 9B, left) may be the result of mutual stress transfer between the aseismic slip on the fault matrix and the foreshock asperities, which eventually focus around the nucleation point to reach the characteristic length at which slip accelerates and unfolds in the main rupture (*67*, *68*). Only a few cases have been documented in subduction zones, where slow slip (or aseismic preslip) appears to penetrate or be very close to the nucleation zone, such as the 2011 Tohoku (*2*, *62*) and 2014 Iquique (*32*, *69*, *70*) megathrust earthquakes.

During the first 2 months following the 8 September earthquake, the postseismic slip completely sweeps the rupture zone reaching depths of less than 10 km (Fig. 8E, fig. S18F, and movie S1). In that period, there is an outstanding reactivation of repeater sequences to the east and south of the rupture where the afterslip develops (Fig. 9B, right). Beginning in November, a large long-term SSE (M_w7.3 and maximum slip of ~22 cm; Fig. 10A) develops mainly between 20 and 45 km in depth (Fig. 8F and fig. S18G) and lasts until April 2022. However, in its late phase, between December and April 2022, the SSE grows, pervading shallow depths offshore of 10 to 15 km along the entire seismic gap to the southwest of Acapulco (Fig. 8G and fig. S18H). Although dominant below 25 km, the long-term SSE outstandingly overlaps to the east with the 1957 and 1989 rupture areas (Fig. 2A), where most of the Acapulco earthquake aftershocks occurred. Although this region appeared ripe for failure in the 10 to 20 days after the earthquake, a doublet similar to that in 1962 never happened (Fig. 9A, right, and movie S2). The updip propagation of long-term SSEs in Guerrero has been observed previously (*25*, *33*, *50*). What we were previously unaware of was the existence of shallow SSEs and their role in the seismogenesis of potentially devastating earthquakes within the gap, which, as described earlier, seems fundamental.

From April 2022, the offshore region south of Acapulco reactivates to initiate the second shallow SSE that may have reached the oceanic trench (M_w7.1; Figs. 8H and 10A and fig. S18I). Then, between July and September 2022, during the 3 months before the M_w7.7 Michoacán earthquake some 350 km to the west (Fig. 1), the SSE evolves to activate a 230-km-long offshore strip between 8 and 25 km in depth that spans the entire seismic gap and the Costa Chica of Guerrero (i.e., east of Acapulco), with maximum slip of 4 cm northwest of OBO5, where the CFS exceeds 70 kPa (Fig. 8I and fig. S18, I and J). The strip has a distinctive shape, characterized by a deeper profile in the west along the gap, where the long-term SSE penetrated onshore regions following the earthquake (similar to the first shallow SSE event; Fig. 10A). This depth profile transitions to a shallower interface region in the east along the Costa Chica, where the slip occurred entirely offshore and encompassed the rupture areas of 1957 and 1989 (fig. S18J). As occurred before the Acapulco earthquake (Fig. 10B), on the edge of the M_w7.7 Michoacán rupture, the deep part of the interface (>40 km) is also reactivated (fig. S18J and movie S1). In this regard, please further note how the tilt in the Cocos plate (OBT7) is strongly accelerated in that 4-month period (Fig. 8I and movie S1) as occurred before the

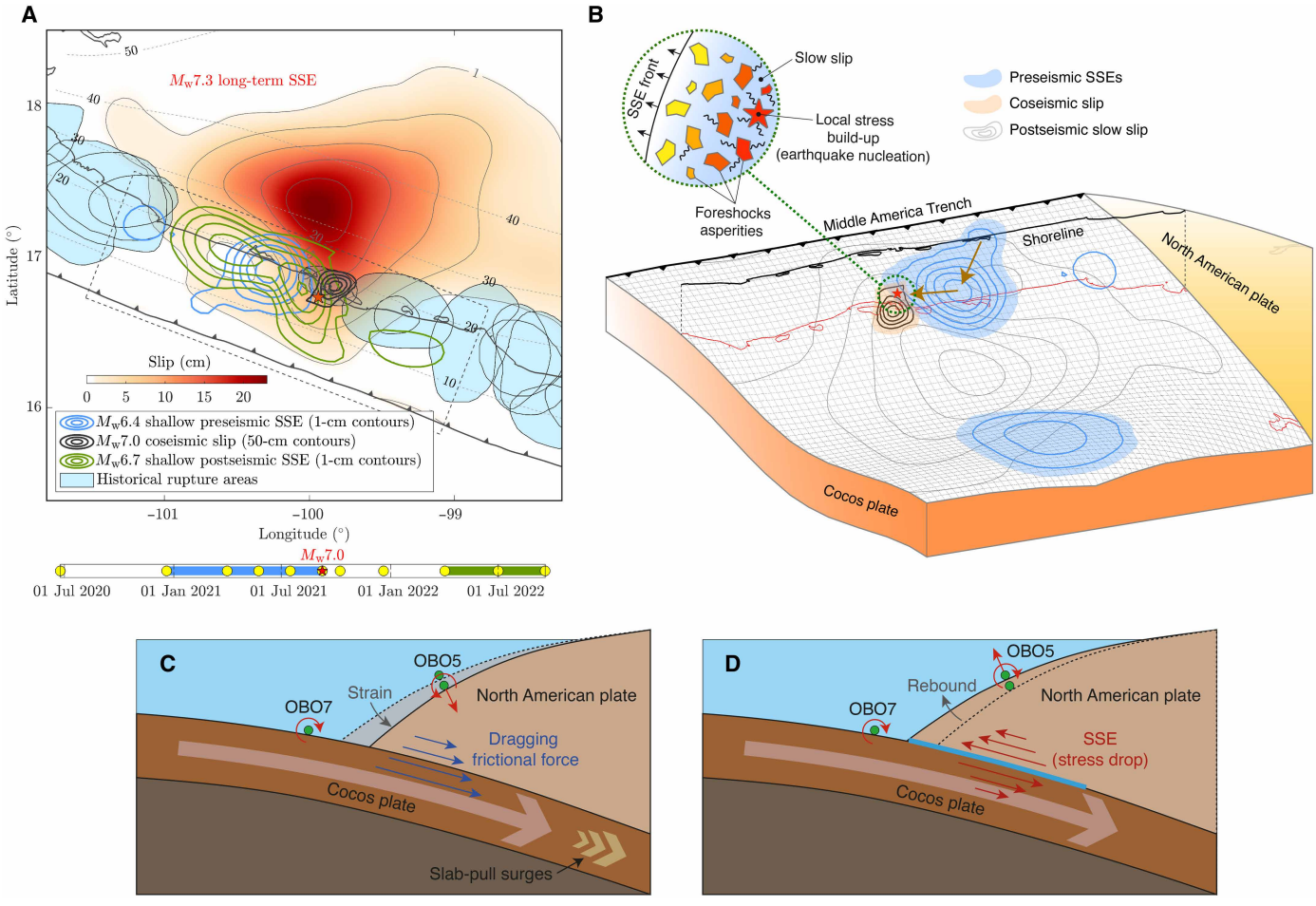

Fig. 10. Summary of the Guerrero gap plate interface activity and explanatory features of seafloor deformation patterns. (**A**) Slip associated with the two shallow SSEs (blue and green contours) together with the cumulative slip (red to orange shade) over the 6.9 months after the Acapulco earthquake (i.e., between 8 September 2021 and 2 April 2022; see bottom timeline). (**B**) Shallow and deep preseismic slow slip (blue shading) over the 8.7 months preceding the earthquake, together with the coseismic slip and hypocenter (red star) of the M_w7.0 rupture. The inset shows the preseismic SSE invasion of the hypocentral region and the local stress concentration on foreshock and mainshock asperities. The gray contours show the M_w7.3 postseismic slow slip. (**C** and **D**) Seafloor deformation patterns (displacement and tilt) in the oceanic and overriding plates during an inter-SSE period (left) and a shallow SSE (right).

M_w7.4 Huatulco (~430 km east; Fig. 1) and M_w7.0 Acapulco earthquakes (see red-shaded transients at OBT7 in Fig. 7B), suggesting a regional episodic activation of the subducted slab, possibly related to the occurrence of the three earthquakes.

A comprehensive summary of the seismic gap activity is presented in Fig. 10A. The most notable observation is the along-strike continuity between the historical rupture areas and the two shallow SSEs discovered here. Our results reveal that the locked seismogenic depths outside the seismic gap align with these short-term slow slip earthquakes within the gap. This indicates that the concept of locked depths in the gap, as commonly understood, may require reevaluation. The baseline of background seismicity in this segment (M > 3.2), between Papanoa (101°W) and Acapulco (100°W), is substantially heterogeneous along the strike (fig. S23A). In the eastern half of the segment, where the two shallow SSEs intersect, seismicity rate is about 10 times higher than observed in the western half, where two M_w6.1 and M_w6.5 events occurred a few weeks after the M_w7.3 Papanoa earthquake west of the gap in 2014 (*71*). Thus, mechanics of the interface to the east seems more prone to slow slip and small ruptures (and repeaters; see Fig. 9B, right) than the western part. Further study is required to confirm this hypothesis, but the evidence suggests that SSEs in the gap do not inhibit the occurrence of small to moderate seismicity compared to segments where M7+ earthquakes occur regularly. The lack of large ruptures within the gap over the past 113 years can be attributed, at least in part, to the occurrence of recurrent episodes of aseismic energy release at shallow depths (i.e., short-term shallow SSEs).

Moreover, the presence of a relatively silent zone offshore in the western sector of the gap (*22*) (fig. S23A, red dashed rectangle), coupled with the observation of tremor in the vicinity of the trench, provides further evidence to this scenario where slow dynamics prevails and fast instabilities are seldom large. Nevertheless, although unlikely as evidenced by the historical record, the potential for large ruptures in the gap resulting from short- and long-term constructive strain interactions and dynamic rupture effects cannot be discounted. This study (see, for instance, the cumulative CFS in fig. S18) and considerations from other regions (*2*, *51*, *72*) provide evidence to support this scenario.

In view of the uncertainty surrounding the tilt baseline at OBT8 due to the absence of a long-term, steady period of observation, as elucidated previously (fig. S15, bottom right), it is pertinent to inquire whether the second shallow SSE truly occurred south of Acapulco (Fig. 8H). The tilt baseline period was selected to ensure consistency between the tilt direction at the station between April and July 2022 and the seaward and downward GNSS displacement at the closest sites (fig. S18I). Nevertheless, this decision is somewhat arbitrary and may result in implausible outcomes. To address this issue, inversions were performed for the final two windows during which OBT8 was operational, with the tilt data excluded. Figure S19 (I and J) illustrates a comparison of the slip solutions when inverting GNSS data alone (on the left), GNSS data combined with OBP data (in the middle), and GNSS data combined with tilt data (on the right). The solutions with and without tilt in the first window are found to be highly similar in the region south of Acapulco, due to the absence of an OBP in the vicinity. They both identify an offshore SSE with a peak value of ~1.5 cm. A similar conclusion can be drawn with regard to the final window (fig. S19J), where the long SSE strip identified in our preferred solution (Fig. 8I and fig. S18J) emerges in all instances, albeit with some variations to the west and southeast of Acapulco. Consequently, the baseline period selected for OBT8 appears to be a reasonable choice, given that independent inversions yielded comparable results, with all observations satisfactorily explained.

During the last window, between 1 July and 18 September 2022, preceding the M_w7.7 Michoacán earthquake about 350 km to the west (Fig. 1), our preferred slip solution (fig. S18J, as well as the three independent ones, fig. S19J) features a large dislocation close to the western limit of our inversion domain. While the closest GNSS data (e.g., ZIHU station) is well explained and the CFS is high (above 50 kPa; fig. S18I), our model lacks resolution in that sector (fig. S16). Therefore, further investigation is necessary to confirm what occurred near the Guerrero-Michoacán states boundary in that period. A similar situation happens in the window preceding the Acapulco earthquake, between 16 July and 8 September 2021 (fig. S18, E and F). During this period, a large slip patch emerges in the eastern region of the domain. Although the resolution at this end is also inadequate, an independent analysis of GNSS data from Oaxaca during this period corroborates the presence of a long-term SSE in the state, as evidenced by the southwestward displacements at TNMQ and OMTS stations in the vicinity of the Oaxaca border.

Near-trench deformations and deep slab activation

As far as we know, the long-standing continuous data from our OBTs are without precedent globally. In light of these observations, it becomes necessary to consider the potential role of tectonic processes that have been rarely observed in the preparation of large ruptures at a regional scale. Figure 10 (C and D) illustrates a segment of the seismic cycle in which an SSE occurs in the vicinity of the trench. During an inter-SSE period, deformation of the forearc resulting from subduction and coupling at the interface causes a distinct displacement and tilt of the ocean floor, as illustrated at station OBO5 in Fig. 10C. In this period, the station sinks and tilts in the trench direction, as evidenced by the data at that site (see the associated wind rose histogram in Fig. 7A), which are predominantly opposite to the plate convergence. When an SSE below occurs and continental rebound takes place (Fig. 10D), the deformation reverses the directions of the observables at OBO5, which implies tilt reversals (and uplift) also present in the histogram with the direction of convergence (associated with the negative slopes at OBT5 in Fig. 7B).

During the initial phase of the tilt transient preceding the Acapulco earthquake (Fig. 7B, red shade), OBT7 starts accelerating with negative slopes (shoreward tilt), while OBT5 accelerates with positive slopes (tilt toward the trench; pattern also found in the first and second transients and within the fourth transient from the M_w7.7 earthquake). The collocated hydrostatic pressure at OBP5 indicates a sinking trend, which aligns with the stage depicted in Fig. 10C (the same situation is clear in the second transient). During the second half of the transient, when OBT7 begins to decelerate, OBT5 reverses the sign of the slope in a similar manner to OBP5, where an uplift occurs. Both reversals are associated with the previously identified offshore SSE (Fig. 8, B to D) (stage corresponding to Fig. 10D). Although of a smaller amplitude, the tilt at OBT4 in this third transient behaves in a similar manner to that observed at OBT5. The disparity in amplitude is likely due to the low interface coupling adjacent to the trench (Fig. 6) and, thus, to the deficit of stored elastic energy in the forearc front. These observations strongly suggest the existence of a causal relationship between transient processes occurring in the oceanic subducted plate and deformations observed in the forearc.

If we accept the existence of a causal relationship between observations made at OBT7 (Cocos plate) and those made at OBOs seated in the forearc, then one is prompted to consider which process may be responsible for triggering the observed phenomena. The prevalent hypothesis would suggest that the slab converges at a constant velocity (in its deep part by asthenospheric drag) and deforms as a function of its interaction with the overriding plate (i.e., as a function of coupling and hence the slip velocity at the plate interface). Thus, a change in interface mechanics (e.g., velocity weakening) would result in a slab rebound and shallow tilt. In this instance, the tilt accelerations observed in OBT7 (Fig. 7B) can be attributed to a change in interface friction and the subsequent elastic response of the oceanic crust to this change. Nevertheless, the available evidence suggests a different outcome because, in that case, tilt at OBT5 would increase in the shoreward direction, as illustrated in Fig. 10D, which is not the case in any of the transients (with the exception of the months before the M_w7.7 Michoacán earthquake, when the second shallow SSE took place). Note that tilt at OBT7 (Cocos plate) exhibits a similar preseismic acceleration before the M_w7.4 Huatulco, M_w7.0 Acapulco, and M_w7.7 Michoacán earthquakes. The most reasonable explanation for the simultaneous increase in the tilt rate at OBT5 toward the trench (positive slope) and the tilt rate at OBT7 in the opposite direction (negative slope) during the initial phase of the transients seems to be that the slab subduction rate increased and friction at the interface remained stationary, thereby enabling the deformation of the forearc according to the evidence from the data. In this scenario, the forearc tilt is a consequence of the deformation transferred through plate coupling due to the slab underthrusting acceleration (a mechanism similar to that illustrated in Fig. 10C).

The episodic tilt acceleration of the Cocos plate (OBT7) observed several months before three regional M7+ earthquakes (with the exception of the initial transient, where a long-term SSE occurred instead) suggests the potential for extended slab episodic processes to precede large regional ruptures. This hypothesis is consistent with the simultaneous activation of shallow and deep SSEs before the 2021 Acapulco (Fig. 10B) and the 2022 Michoacán (fig. S18J) earthquakes, which demonstrates that the slab experienced acceleration along the

entire subduction channel before these ruptures. In summary, the observed tilt and hydrostatic pressure data in both the Cocos and forearc near-trench regions suggest that the slab was subjected to transient alterations in its subduction velocity before three earthquakes, lasting between 4 and 8 months, which may be regarded as precursory "slab-pull surges" (SPSs).

A similar idea to that of precursory SPSs introduced here was previously advanced by Bouchon *et al.* (*73*) based on the analysis of foreshock seismicity before the 2010 Maule, 2014 Iquique, and 2011 Tohoku megathrust earthquakes. The synchronous occurrence of shallow thrust foreshocks and deep intraslab normal ruptures led these authors to postulate a causal relationship between both kinds of seismic events, rooted in the transient stretching of the slab deep into the mantle. Months before the Maule and Tohoku ruptures, GNSS observations by Bedford *et al.* (*74*) also identified a several-month-long transient deformation across thousands of kilometers and a sudden pulldown of the slab, potentially caused by the rapid and deep densification of metastable minerals within the oceanic plate. This model for the Tohoku earthquake preparation is further supported by the massive gravity anomaly found by Panet *et al.* (*75*) months before the rupture, which indicates a regional-scale mass redistribution within the mantle announcing the earthquake. The periodic acceleration of the interface slip, as inferred from repeating earthquakes in eastern Japan, and its correlation with the occurrence of large earthquakes point in the same direction (*65*), where transient processes within the slab perturbing the subduction velocity cause the ruptures. All these findings embrace the idea of SPSs as a potentially universal precursor of large to great ruptures, which are inferred from the near-trench oceanic-crust tilt episodes preceding three M7+ regional earthquakes in Mexico.

The ocean-bottom instruments that provided the data for this study were installed in November 2017 (*5*), 2 months after the M_w8.2 intraslab Tehuantepec earthquake of 8 September 2017. In the aftermath of that earthquake, the largest ever recorded in Mexico, the mechanical properties of the plate interface underwent alterations on a regional scale (*33*). That is, the instruments were deployed during the period of peak mechanical disturbance of the interface. The unprecedented seismic waves caused dynamic stress perturbations of ~100 kPa for over 70 s at the interface in the vicinity of Acapulco, more than 600 km away (*33*). These transient perturbations triggered an SSE in Oaxaca and markedly disrupted the periodicity and magnitude of SSEs in Guerrero over the subsequent 2 years (*33*). Five months after the rupture, on 16 February 2018, another earthquake (M_w7.2; Fig. 1) was triggered near Pinotepa Nacional by the unfolding Oaxaca SSE (*33*). Figure 7A illustrates the tilt time series at the three operational stations at that time (OBT4, OBT5, and OBT7) together with the timing of the aforementioned ruptures. From the M_w7.2 Pinotepa earthquake onward, there was a marked change in the tilting tendency of the forearc (OBT4 and OBT5) over the following 4 months. It is noteworthy that OBT4, situated 9 km from the trench and characterized by long-term stationary behavior, experienced an unparalleled tilt change of ~1 μrad in the trench direction (positive slope) during this period. A similar but smaller transient is also present right after the Michoacán earthquake in 2022. At the same time, from the M_w7.2 rupture, OBT5 undergoes a transient tilt reversal in the opposite direction, toward the coast (negative slope). Dynamic perturbations generated by the Pinotepa earthquake (of the order of 70 kPa for ~10 s at the interface near Acapulco), with an epicenter 250 km east of the subsea network, triggered a deep SSE on the Costa Chica of Guerrero (north-northwest of Acapulco) (*33*), spanning the same period as the tilt transients (blue shade). The Cocos plate (OBT7), on the other hand, experienced the highest tilt rate in a long time following the Pinotepa earthquake. Preliminary inversion of these signals, which is beyond the scope of this work, reveals that the Pinotepa earthquake also triggered an SSE offshore, in close proximity to the trench. The more comprehensive investigation currently underway, which has also identified contemporary tectonic tremor in ocean bottom seismometers (*22*), underscores the necessity of ultralong-period TMAs on both tectonic plates to detect SSEs that may also be triggered dynamically by seismic waves from regional earthquakes. These findings will contribute to our understanding of the mechanical response of the interface associated with frequent large events and, thus, to our comprehension of their role in the evolution of the seismic cycle.

The observation of SSEs offshore and precursory SPSs in the oceanic crust was made possible by affordable TMAs, that is, unprecedented seafloor instruments that enable the detection of near-trench tilt transients, presumably linked to deep processes within the slab. These instruments can detect signals beyond the reach of substantial ocean noise, which can seriously obscure tectonic deformations in ultrasensitive sensors such as OBPs and existing OBTs. Continuous monitoring of the seafloor tilt using TMAs, at both the incoming and overriding plates, could prove invaluable in identifying short-term processes and patterns that lead to SSEs and/or large regional ruptures at a smaller scale than the aforementioned megaruptures in Japan and Chile. Tilt data from all the Fetch units (or similarly design devices) deployed in different subduction zones such as New Zealand, Alaska, the Sea of Marmara, Cascadia, and Chile can already be used to do this systematically. The prospective development of future laboratory-designed TMAs with preestablished amplification responses in conjunction with submarine cable systems or real-time satellite data transmission has the potential to markedly enhance our capacity to observe the precursors of and to forecast future catastrophic earthquakes and tsunamis.

MATERIALS AND METHODS

Acapulco earthquake coseismic slip inversion

For the inversion, we assumed a planar fault discretized with 2-km subfaults, with the W-phase focal mechanism provided by the US Geological Survey (i.e., strike 279°, dip 20°, and rake 73°) and a relocated hypocenter at a latitude of 16.77° and a longitude of −99.94° with a depth of 16 km (*47*). Furthermore, a von Karman correlation length of 10 km with a Hurst exponent of 0.75 was assumed to spectrally bound the inversion. With a maximum recorded uplift of 20.3 cm at station ACAP (fig. S2), our preferred source model produced a root mean square (RMS) misfit of 0.74 ± 0.47 cm and 0.41 ± 0.28 cm for the GNSS and InSAR data, respectively (Fig. 2 and fig. S4), while mobile checkerboard (MOC) resolution tests indicate that the model has a nominal error under 10% within the rupture area for slip patches larger than 10 km [i.e., median restitution indexes (MRIs) above 0.9; fig. S5].

Analysis of OBP data

Seafloor hydrostatic pressure is primarily a superposition of harmonic functions (fig. S6A) associated with ocean tides that can therefore be removed from the records by subtracting theoretical tidal predictions (*40*) or by filtering data (fig. S6, B and C). However,

nontidal oceanographic components related mostly to ocean currents, gyres, and eddies resulting from the wind blowing across the ocean and by differences in the water temperature, density, and atmospheric pressure represent noise whose amplitude may exceed those expected from small tectonic deformations (*41*, *76*, *77*).

At our three long-standing sites, OBP4, OBP5, and OBP7, a comparison between filtered pressure for different high-pass periods, T, and temperature (fig. S7C) shows that a substantial correlation exists only at the shallowest site, OBP5, with 973 m in depth [i.e., maximum correlation coefficient (*cc*) of 0.44 around $T = 35$ days] (fig. S7A). The time lag that maximizes correlation in that site is 12 days (with delayed temperature) but ranges between 9 and 14 days for $10 < T < 60$ days (fig. S7B). In contrast, on the deepest sites OBP4 (2374 m in depth) and OBP7 (4992 m in depth), the maximum *cc* is below 0.31 for all cutoff periods and the associated lags around 18 and 150 days, respectively. Thus, for the analysis, we correct the pressure data at OBP5 only by subtracting the scaled temperature with the time lag that maximizes *cc* (*42*), where the scaling factor is the quotient between the RMS of the pressure and the temperature. Figure S8 illustrates how important the temperature correction is at OBP5 relative to the reference site OBP7 on the incoming Cocos plate. Corrected signals (right column) are very consistent regardless of the frequency band and substantially less noisy in long periods. In addition, as discussed in the "Transient forearc deformation: Offshore and onshore data" section, the data local trends in the corrected signals are much more consistent in time and space with seafloor tilt and GNSS observations.

TMA model

Figure 5A shows a two-dimensional free-body diagram of a tilted unit seated upon marine sediments. The exact technical specifications and dimensions of the units are given in fig. S10 and table S1. Assuming a rigid basement and tripod, to find forces $\mathbf{F}_1(\alpha)$ and $\mathbf{F}_2(\alpha)$ during the quasi-static instrument tilt α, we first assume that angular moments from all existing forces vanish. Equilibrium of angular moments with respect to the feet of leg 1 and leg 2 reads

$$\sum M_{F_1} = W\frac{L}{2}\cos\alpha - Wh\cdot\sin\alpha - F_{1N}\cdot L = 0 \Longrightarrow F_{1N} = W\cdot A_1 \quad (1)$$

and

$$\sum M_{F_2} = -W\frac{L}{2}\cos\alpha - Wh\cdot\sin\alpha + F_{2N}\cdot L = 0 \Longrightarrow F_{2N} = W\cdot A_2 \quad (2)$$

respectively, where

$$A_1 = \frac{1}{2}\cos\alpha - \frac{h}{L}\sin\alpha$$

and

$$A_2 = \frac{1}{2}\cos\alpha + \frac{h}{L}\sin\alpha$$

If we neglect basement deformations between legs in the x-axis direction (i.e., strain tensor component $e_{xx} = 0$, which implies constant displacement u_x) and thus assume that tangential forces in both feet are given by Amonton's law, then

$$F_T = m\,F_N \quad (3)$$

where m is the friction static coefficient, and the equilibrium of forces in the x-axis direction reads

$$\sum F_x = \mu\left(F_{1N} + F_{2N}\right) - W\cdot\sin\alpha = 0$$

Arranging terms after substitution of Eqs. 1 and 2 yields

$$W(\mu\cdot\cos\alpha - \sin\alpha) = 0 \quad \mu = \tan\alpha \quad (4)$$

Magnitude of force $\mathbf{F}_i$, where $i \in [1, 2]$, is given by

$$|\mathbf{F}_i(\alpha)| = \sqrt{F_{iT}^2 + F_{iN}^2}$$

so that Eqs. 1 to 4 lead to the general expressions for both legs' forces

$$|\mathbf{F}_i(\alpha)| = WA_i\sqrt{1 - \tan\alpha^2}$$

which simply reduces to

$$|\mathbf{F}_i(\alpha)| = W\left(0.5 \pm \frac{h}{L}\tan\alpha\right) \quad (5)$$

where $i = [1, 2]$ stands for leg 1 and addition or leg 2 and subtraction, α for the basement (i.e., tectonic) tilt, W for the unit net weight under the water, h for the height of the glass sphere, and L for the leg aperture at the basement. Since the expected tilt during an SSE is small (i.e., tens of microradians so that $\tan\alpha \approx \alpha$), Eq. 5 is linear. As expected, for $a = 0$ (horizontality), each force is half the Fetch unit net weight in water, and for $\alpha = \theta = a\tan(L/2h)$ (see Fig. 5A), $\mathbf{F}_1 = W$ and $\mathbf{F}_2 = 0$.

Thus, for small α, both forces are linear functions of tilt with opposite signs. This means that a tilt increment implies an increment of $\mathbf{F}_1$ and a decrement of $\mathbf{F}_2$ of the same magnitude. Considering the mass and buoyancy of all unit components, the net total weight W is 402.2 N (table S1). Given the leg-foot surfaces of 0.108 m^2, the unit would exert an initial pressure P_0 of 1.862 kPa on each leg for $\alpha = 0$ (horizontal case). However, since the actual tripod is three dimensional (i.e., it has three legs; fig. S10B) and tilt can be at any azimuth, to mitigate the two-dimensional simplification, we multiply the forces by a factor of 2/3 in subsequent analysis.

Deepwater marine sediments are highly compressible (*54*, *55*, *78*). Under a quasi-static load, their volume undergoes large changes due to fluid drainage and particle consolidation. One way of quantifying this is by estimating the distribution of vertical stresses across the sediment column and the corresponding settlement. Boussinesq (*79*) introduced a model describing the vertical stress in a soil produced by a distributed circular load on top of it, which reads

$$\Delta\sigma_z = q\left[1 - \left(\frac{1}{1 + \left(r_0/z\right)^2}\right)^{3/2}\right] \quad (6)$$

where q is the load pressure, r_0 is the radius of the load, and z is the depth. In our case, $r_0 = 0.1854$ m (deduced from table S1) and $q = P_0 = 1.862 \times \frac{2}{3} = 1.242$kPa on each leg for $\alpha = 0$ μrad. The blue curve of fig. S11A depicts the corresponding $\Delta\sigma_z$ as a function of depth. The total stress, σ_{tot}, will be the sum of $\Delta\sigma_z$ and the effective vertical stress, σ_{eff} or γ, which grows linearly with depth and ranges between 2.5 and 10.2 kPa/m in deep, water-saturated seabed clay

samples (*54*). The black and red curves in fig. S11A show σ_{eff} and σ_{tot}, respectively, assuming the average value $\gamma = 5$ kPa/m reported by Davie *et al.* (*54*).

As a first-order approximation, the settlement (i.e., the normal surface displacement due to sediment consolidation) of a water-saturated layer with thickness H_0 may be estimated as (*80*)

$$\delta = C_c \frac{H_0}{1 + e_0} \log \frac{\sigma_{tot}}{\sigma_{eff}} \quad (7)$$

where C_c is the sediments compressibility index and e_0 the associated void ratio. Consolidation tests on different types of marine sediments from the Gulf of Mexico and the Pacific Ocean indicate that C_c may vary substantially, ranging within 0.25 to 0.7 for terrigenous clays, within 0.66 to 1.2 for diatom-rich terrigenous clays, and within 1.7 to 1.82 for hemipelagic and pelagic clays (*54*, *55*). Values for e_0 determined by these authors range between 0.7 and 1.7 and 3.5 and 6.0 for the first and third kinds of clays, respectively. The larger C_c and the smaller e_0, the higher the settlement will be. Given a depth discretization of n thin layers with thickness $H_0 = \Delta z$, we can estimate the settlement δ at any depth z by integrating Eq. 7 for layers deeper than or equal to z. Our long-record Fetch units are settled at ~1000 m (OBO5 and OBO8, continental slope), 2374 m (OBO4, nearby continental rise), and 4992 m (OBO7, abyssal plain) in depth, so they were likely on top of different kinds of clays. However, since we do not have any information about the actual properties of sediments at each OBO site, to illustrate the procedure, we set $C_c = 1.1$ and $e_0 = 4.2$, which are not extreme values and thus lead to conservative estimates.

Figure S11B shows the settlement associated with the stress condition of fig. S11A. Equations 6 and 7 involve nonlinear functions, so that settlement decreases rapidly with depth, being 35.2 mm at the surface and about an order of magnitude less at 0.5 m in depth. This estimate corresponds to the initial load $q = P_0$ under each unit leg for $\alpha = 0$ μrad (horizontal case). In the absence of sediments, Eq. 1 predicts linear differential increments of the legs' pressure with tilt. However, once the basement begins to tilt (i.e., for $\alpha \neq 0$ in Eq. 1), the differential pressure upon the sediments induces differential settlements that are nonlinear functions of the evolving Boussinesq stress (Eq. 6) and settlement (Eq. 7). This means that the tectonic tilt is no longer linearly related to the pressure of the legs acting upon the sediments. Because of suction effects on leg 2 where the pressure decreases, in the following, we assume that no displacement occurs there so that the settlement-induced tilt, α_s, will be only due to consolidation beneath leg 1, where pressure increases. Furthermore, since we are interested in slow tectonic deformations that may last from weeks to several months, we also assume that settlement evolves quasi-statically, which means that any fluid drainage/diffusion effects occurring on smaller timescales are neglected. This also implies that possible restoring processes in the sediments associated with suction effects where pressure decreases are not considered. Although beyond the scope of this study, the evaluation of these processes may be important because they could demonstrate the long-term viability of TMAs on the ocean floor.

To quantify the evolution of α_{tot}, the effective instrument tilt within the glass sphere, as the basement tilts, we solve iteratively for δ as α increases linearly from 0 to 2.5 μrad with steps $\Delta\alpha = 0.03$ μrad. This means that for every ith α step, we (i) use α^i_{tot} to estimate pressure P_1 on leg 1 (Eq. 5), (ii) estimate the incremental pressure $\Delta P = P_1 - P_0$, (iii) estimate the incremental total stress $\Delta\sigma^i_{tot}$ from ΔP (Eq. 6), (iv) estimate the incremental settlement $\Delta\delta^i$ from $\Delta\sigma^i_{tot}$ (Eq. 7), (v) estimate the incremental settlement-induced tilt $\Delta\alpha^i_s$ as $\arctan(\Delta\delta^i)$ (because $L = 1$ m; table S1), and (vi) update the effective instrument tilt as $\alpha^{i+1}_{tot} = \alpha^i_{tot} + \Delta\alpha + \Delta\alpha^i_s$ before stepping forward.

Tilt data analysis

As previously described by Villafuerte *et al.* (*51*) for the treatment of GNSS time series, the right column of fig. S12 presents the tilt dataset after the removal of outliers exceeding ±1.5σ of the mean difference with a locally weighted second-order polynomial regression (red curves) with a moving support of 250 samples. This procedure is important to accurately determine the sensors' orientation and does not affect the general data trends. Note that regressions were run independently on every earthquake-bounded segment so that tilt discontinuities produced by the events could be seen.

Except for OBT4, which is seated on the North American plate about 9 km from the oceanic trench, the time series show a clear long-term trend. Besides, they all show month-long transient variations most time correlated with the previously documented 2018 and 2019 long-term SSEs in Guerrero (*33*) and the 2021–2022 events. To assess the origin of these variations, we first compared both tilt components in the three long-recording sites with collocated temperatures (fig. S13A) and hydrostatic pressure (fig. S13B) for different period bandwidths. As for the pressure-temperature analysis, to quantify the correlation between the observables, we (i) detrended the tilt data, (ii) normalized the temperature and pressure so that their RMS is equal to the tilt's time series, and (iii) search for the moveouts maximizing the correlation coefficients (*cc*). The lack of similarity between the tilt and pressure/temperature time series is quantitatively confirmed (fig. S13C) with *cc* less than 0.16 in all cases except for pressure in OBT7, where it reaches an average of ~0.27, well below the correlation found between pressure and temperature in OBP5 (fig. S7). These results are somehow expected because the tiltmeters are isolated from the water within the glass sphere and point toward a possible link between the tilt variations and tectonic activity. Another possible origin of the variations could be local soil settlements and/or landslides. However, as shown in the "SSE-induced seafloor tilt" section, most of them are correlated in time between sites more than 20 km apart, which rules out these hypotheses in those cases.

To estimate the orientation of the tiltmeters, for the 3.5-year data windows between 17 February 2018 and 7 September 2021, we assumed that the first eigenvector of the data covariance matrix at each site is parallel to the plate convergence with respect to North America [according to the NUVEL-1A model (*57*)], which has an azimuth of 35.5° from the North on the Middle America trench at the traverse of Acapulco. This hypothesis is important because it implies that the long-term data trends are driven by the secular deformation of the crust produced by the subduction of the Cocos plate underneath the continent. It is noteworthy that tests with substantially shorter windows (i.e., of several months) yielded reasonable results if chosen during quiescent periods. In the case of OBT8, which is located 26 km offshore of Acapulco and has a much shorter record with large time variations, the sensor orientation becomes more difficult. This site was deployed on 3 April 2022, only 7 months after the M_w7.0 Acapulco earthquake and during the subsequent SSE in Guerrero discussed later. Thus, the site was likely tilting fast because of the nearby rupture afterslip and/or the SSE. We tried

different baseline windows looking for correlations with the closest GNSS site ACAP, where the north component changed its trend from April 2022 (Fig. 4A), and found that the baseline from 2 April to 1 June 2022 was the most reasonable choice for the principal component decomposition. However, we do not have strong arguments to validate the sensor orientation at this site, so the data should be treated with caution for interpretation. Another uncertainty in the general procedure is the actual sign of the eigenvectors. Since we do not have any information about the instrument landing orientations, the first eigenvector could have either sign. For this reason, as detailed in the "SSE-induced seafloor tilt" section, we used theoretical tilt predictions for an inter-SSE deformation period to attribute the signs.

Figure S14A (left column) shows the baseline tilt components as a function of time at each site along with the two associated eigenvectors. The eigenvector with the largest eigenvalue, P_1, corresponds to the direction that maximizes the baseline tilt rate. Assuming that this direction corresponds to the plate convergence, we can simply decompose the whole time series into north and east geographic components, as shown in fig. S14B (right column). One of the most prominent features in the geographically referenced signals is the eastward tilt jump at station OBT5 due to the Acapulco earthquake (see Fig. 2A). Figure S15 shows the tilt components in the plate convergence (P_l) and its perpendicular (P_{lp}) directions along with linear regressions indicating the long-term rates (except for OBT8, where there are no long-term data). Notice that tilt rates in the P_l direction at OBT5 and OBT7 are opposite signs because the former lies on the overriding plate and the latter on the subducting Cocos plate. While station OBT4 close to the trench is stable in both components, tilt rates in the P_l direction are much higher in the other three sites, with absolute values ranging from ~400 to ~2000 μrad/year. As expected, because of the sediment-induced tilt amplification, these values are extremely high when compared with known secular deformations of the crust in subduction margins (*44*, *45*).

Inter-SSE plate interface coupling inversion

For the inversion of the inter-SSE coupling from GNSS displacement data, the interface was discretized with 5-km subfaults. Furthermore, a von Karman correlation length of 30 km with a Hurst exponent of 0.75 was assumed. The von Karman correlation function has been extensively studied to characterize the spectral content of the slip produced by multiple earthquakes. The Hurst exponent determines its spectral decay, and it is the value of 0.75 that best describes the observations of past earthquakes. The correlation length modulates the bandwidth and was optimized from several MOC tests. An advantage for the inversion of geodetic data from the Mexican subduction zone compared to Northern Japan and Chile, where the oceanic trench is more than 120 km from the coast, is the proximity that separates them in Guerrero of only ~65 km. This allows remarkably high interplate slip resolution offshore even in the absence of ocean-bottom instruments. Figure S16 shows the result of MOC tests (*50*) for three different checker unit sizes (h; fig. S16, top), considering the three-dimensional interface geometry introduced by Cruz-Atienza *et al.* (*33*). The number of checkerboard inversions for each MOC ranged between 18 and 32 depending on h. The second and third rows of the figure display the MRIs (*50*) excluding and including the vertical displacements at the OBPs (i.e., at OBP4 and OBP5), respectively. In the worst-case scenario where OBPs were excluded for the smallest $h = 40$ km (left column), MRIs are close to 0.7 at the oceanic trench within the GGap. This means that our slip (coupling or SSEs) solutions should have a nominal error below ~30% as compared to the actual slip for patches larger than or equal to 40 km from the oceanic trench up to an interface depth of about 40 km. For larger h equal to 60 and 80 km (middle and right columns), MRI rises to 0.75 and 0.8 at the trench without OBPs and above 0.85 in the best-case scenario for $h = 80$ km including OBPs.

Tilt and displacement joint inversion

ELADIN addresses regularization by iteratively projecting the problem solution into a physically consistent and spectrally bounded space determined by the von Karman correlation function (*50*). The spectral bounds are thus defined by both the Hurst exponent and the correlation length of that function. Well-balanced solutions will also depend on the relative data weights that we systematically explored. Figure S17 shows three checkboard inversions in the absence of noise considering a correlation length of 30 km, a Hurst exponent of 0.75 (both optimal values determined from the MOC tests; fig. S16) and a data weighting that depends on precision matrices derived from each dataset (i.e., GNSS/OBP and tilt). Precision is a data-driven metric incorporated into the ELADIN formalism to penalize unreliable observations and corresponds to the inverse of the data covariance (*50*). In practice, given the independently determined precision matrices for displacement and tilt, which varies between zero and one and thus implies a data weak normalization, we found that a relative average weight of 12:1 between both matrices, being larger the displacement matrix, yields reasonable and stable results. This means that tilt remarkable sensitivity to slip should be compensated to allow displacement illumination of the plate interface across larger wave numbers. Another consideration for properly balancing the inversions is to set all data in units producing magnitudes of the same order, i.e., displacement in centimeters and tilt in microradians. The checkerboard inversions in fig. S17, whose target model intentionally includes slip at the trench (fig. S17A), were obtained following this strategy for GNSS data alone (fig. S17B), for GNSS and OBP data (fig. S17C), and jointly for GNSS, OBP, and tilt data (fig. S17D). While the three tests resolve similarly well the slip distribution onshore, only the inversion including tilt is able to retrieve the target model up to the oceanic trench. The relative weight between displacement and tilt is particularly important and should probably depend on the tectonic context and/or the inversion formal strategy used.

The left column of fig. S18 shows the joint inversion and model data fit of GNSS, OBP, and tilt observations for the 10 windows (yellow dots in Figs. 4A and 7A) carefully selected on the basis of the behavior of data from 24 June 2020 to 18 September 2022. During those 2.2 years surrounding the M_w7.0 Acapulco earthquake, several remarkable events took place. Note that the first 6-month window corresponds to a rather quiescent inter-SSE period. To better appreciate the events, we time interpolated the solutions every 10 days by means of piecewise cubic Hermite interpolating polynomials, which honor the target function when providing a more physically consistent picture of slip (e.g., its acceleration) than simple piecewise linear regressions. We stress that no substantial change in the interpretation of the solutions depends on our chosen interpolant.

TM analysis

The TM technique we used was introduced by Liu *et al.* (*63*). The technique was applied over 3-year-long continuous records at eight

broadband seismic stations distributed in Guerrero (inset in Fig. 1) from 1 January 2020 to 31 December 2022. The templates correspond to waveforms of 4876 earthquakes reported by the Servicio Sismológico Nacional during the same period. TM performs a continuous search by computing the correlation coefficient between the templates and the data at each sample step. A detection is declared when the stacked correlation coefficient for the three components of five stations exceeds n times the mean average deviation (MAD) of the correlation coefficient for each day. Since the study region is large (i.e., more than 300 km along the coast), the search was divided in two sectors with five stations each and an overlap between them (fig. S20A). By visually inspecting the detections for different MAD threshold values, we empirically determined that a MAD of ≥15 provides a robust and reliable catalog with 38,501 earthquakes (fig. S20C). Representative examples of waveforms matches are shown in fig. S21 along with the associated MAD values. Following Liu *et al.* (*63*), the magnitude of the detections was estimated by comparing the median of the relative amplitude between the peak values of the template and the detection. The maximum curvature criterion of the Gutenberg-Richter distribution leads to a completeness magnitude $M_c = 3.1$ (fig. S20B). The location of each detection was attributed following a three-dimensional normal distribution centered at the template location with an SD of 0.03° horizontally and 3 km in depth, so that most of detections from a single template lie within a spheroidal region with ~7-km radius (i.e., 2 s).

Background seismicity baseline

To establish the background seismicity baseline, the seismic catalog was spatially discretized on a regular grid of 15 km per side (fig. S20C) to estimate temporal linear regressions in each bin of the grid. To loosely guarantee the completeness of the catalog, only earthquakes with magnitude greater than or equal to 3.2 were considered. Figure S23A shows the baseline determined along with the region where the regressions have an adjusted R^2 value greater than 95%, derived from the spatial distribution of that metric shown in fig. S23B. That is, the region where the linear model is reasonably representative of the background seismicity rate. To illustrate the validity of the approach, fig. S23 (C and D) shows the earthquake cumulative counts along with the baseline linear models at five selected sites and in a 20-km-radius region around the hypocenter of the Acapulco earthquake, respectively. To estimate seismicity rate deviations from the baseline between 1 April 2021 and 18 September 2022, the period following the tectonic quiescence, a temporal scan of the catalog was performed in 10-day increments to subtract the baseline from the rate determined per window in each bin. The evolution of the seismicity rate deviations is shown in movie S2 along with the slow slip contours and the occurrence of repeating earthquakes.

CFS and seismicity rate

The CFS associated with each individual slip inversion (fig. S18) was interpolated every 10 days in the same manner as done for the slip (movie S1). Figure S24 (B to D) compares the seismicity rate time series with the slip rate (left column) and CFS rate (right column) time series, averaged over three circular regions R1, R2, and R3 with a radius of 20 km (fig. S24A), a length that corresponds to the characteristic asperity size resolved above 80% in our near-shore slip inversions (see fig. S16, left column). The top panels in fig. S24 (B to D) show the cross-correlation coefficient (*cc*) as a function of time for the associated time series below using a wavelet decomposition approach (*81*).

Supplementary Materials

The PDF file includes:
Figs. S1 to S24
Tables S1 and S2
Legends for movies S1 and S2

Other Supplementary Material for this manuscript includes the following:
Movies S1 and S2

REFERENCES AND NOTES

1. S. Aoi, Y. Asano, T. Kunugi, T. Kimura, K. Uehira, N. Takahashi, H. Ueda, K. Shiomi, T. Matsumoto, H. Fujiwara, MOWLAS: NIED observation network for earthquake, tsunami and volcano. *Earth Planets Space* **72**, 126 (2020).
2. Y. Ito, R. Hino, M. Kido, H. Fujimoto, Y. Osada, D. Inazu, Y. Ohta, T. Iinuma, M. Ohzono, S. Miura, M. Mishina, K. Suzuki, T. Tsuji, J. Ashi, Episodic slow slip events in the Japan subduction zone before the 2011 Tohoku-Oki earthquake. *Tectonophysics* **600**, 14–26 (2013).
3. E. E. Davis, H. Villinger, T. Sun, Slow and delayed deformation and uplift of the outermost subduction prism following ETS and seismogenic slip events beneath Nicoya Peninsula, Costa Rica. *Earth Planet Sci. Lett* **410**, 117–127 (2015).
4. L. M. Wallace, S. C. Webb, Y. Ito, K. Mochizuki, R. Hino, S. Henrys, S. Y. Schwartz, A. F. Sheehan, Slow slip near the trench at the Hikurangi subduction zone, New Zealand. *Science* **352**, 701–704 (2016).
5. V. M. Cruz-Atienza, Y. Ito, V. Kostoglodov, V. Hjörleifsdóttir, A. Iglesias, J. Tago, M. Calò, J. Real, A. Husker, S. Ide, T. Nishimura, M. Shinohara, C. Mortera-Gutierrez, S. García, M. Kido, A seismogeodetic amphibious network in the Guerrero seismic gap, Mexico. *Seismol. Res. Lett.* **89**, 1435–1449 (2018).
6. E. K. Fredrickson, W. S. D. Wilcock, D. A. Schmidt, P. MacCready, E. Roland, A. L. Kurapov, M. A. Zumberge, G. S. Sasagawa, Optimizing sensor configurations for the detection of slow-slip earthquakes in seafloor pressure records, using the Cascadia Subduction Zone as a case study. *J. Geophys. Res. Solid Earth* **124**, 13504–13531 (2019).
7. G. Barcheck, G. A. Abers, A. N. Adams, A. Bécel, J. Collins, J. B. Gaherty, P. J. Haeussler, Z. Li, G. Moore, E. Onyango, E. Roland, D. E. Sampson, S. Y. Schwartz, A. F. Sheehan, D. J. Shillington, P. J. Shore, S. Webb, D. A. Wiens, L. L. Worthington, The Alaska amphibious community seismic experiment. *Seismol. Res. Lett.* **91**, 3054–3063 (2020).
8. A. M. Tréhu, A. de Moor, J. M. Madrid, M. Sáez, C. D. Chadwell, F. Ortega-Culaciati, J. Ruiz, S. Ruiz, M. D. Tryon, Post-seismic response of the outer accretionary prism after the 2010 Maule earthquake, Chile. *Geosphere* **16**, 13–32 (2020).
9. G. Rogers, H. Dragert, Episodic tremor and slip on the Cascadia subduction zone: The chatter of silent slip. *Science* **300**, 1942–1943 (2003).
10. K. Obara, H. Hirose, F. Yamamizu, K. Kasahara, Episodic slow slip events accompanied by non-volcanic tremors in southwest Japan subduction zone. *Geophys. Res. Lett.* **31**, 1–4 (2004).
11. S. Y. Schwartz, J. M. Rokosky, Slow slip events and seismic tremor at circum-pacific subduction zones. *Rev. Geophys.* **45**, RG3004 (2007).
12. Y. Ito, K. Obara, K. Shiomi, S. Sekine, H. Hirose, Slow earthquakes coincident with episodic tremors and slow slip events. *Science* **315**, 503–506 (2007).
13. Y. Yamashita, H. Yakiwara, Y. Asano, H. Shimizu, K. Uchida, S. Hirano, K. Umakoshi, H. Miyamachi, M. Nakamoto, M. Fukui, M. Kamizono, H. Kanehara, T. Yamada, M. Shinohara, K. Obara, Migrating tremor off southern Kyushu as evidence for slow slip of a shallow subduction interface. *Science* **348**, 676–679 (2015).
14. S. Ide, Variety and spatial heterogeneity of tectonic tremor worldwide. *J. Geophys. Res. Solid Earth* **117**, B03302 (2012).
15. C. Villafuerte, V. M. Cruz-Atienza, Insights into the causal relationship between slow slip and tectonic tremor in Guerrero, Mexico. *J. Geophys. Res. Solid Earth* **122**, 6642–6656 (2017).
16. V. Kostoglodov, A. Husker, N. M. Shapiro, J. S. Payero, M. Campillo, N. Cotte, R. Clayton, The 2006 slow slip event and nonvolcanic tremor in the Mexican subduction zone. *Geophys. Res. Lett.* **37**, L24301 (2010).
17. H. Houston, Low friction and fault weakening revealed by rising sensitivity of tremor to tidal stress. *Nat. Geosci.* **8**, 409–415 (2015).
18. R. D. Hyndman, P. A. McCrory, A. Wech, H. Kao, J. Ague, Cascadia subducting plate fluids channelled to fore-arc mantle corner: ETS and silica deposition. *J. Geophys. Res. Solid Earth* **120**, 4344–4358 (2015).
19. P. Audet, M. G. Bostock, N. I. Christensen, S. M. Peacock, Seismic evidence for overpressured subducted oceanic crust and megathrust fault sealing. *Nature* **457**, 76–78 (2009).

20. E. Warren-Smith, B. Fry, L. Wallace, E. Chon, S. Henrys, A. Sheehan, K. Mochizuki, S. Schwartz, S. Webb, S. Lebedev, Episodic stress and fluid pressure cycling in subducting oceanic crust during slow slip. *Nat. Geosci.* **12**, 475–481 (2019).
21. V. M. Cruz-Atienza, C. Villafuerte, H. S. Bhat, Rapid tremor migration and pore-pressure waves in subduction zones. *Nat. Commun.* **9**, 2900 (2018).
22. R. Plata-Martinez, S. Ide, M. Shinohara, E. S. Garcia, N. Mizuno, L. A. Dominguez, T. Taira, Y. Yamashita, A. Toh, T. Yamada, J. Real, A. Husker, V. M. Cruz-Atienza, Y. Ito, Shallow slow earthquakes to decipher future catastrophic earthquakes in the Guerrero seismic gap. *Nat. Commun.* **12**, 3976 (2021).
23. T. Nishikawa, T. Matsuzawa, K. Ohta, N. Uchida, T. Nishimura, S. Ide, The slow earthquake spectrum in the Japan Trench illuminated by the S-net seafloor observatories. *Science* **365**, 808–813 (2019).
24. T. Nishimura, Y. Yokota, K. Tadokoro, T. Ochi, Strain partitioning and interplate coupling along the northern margin of the Philippine Sea plate, estimated from global navigation satellite system and Global Positioning System-Acoustic data. *Geosphere* **14**, 535–551 (2018).
25. M. Radiguet, F. Cotton, M. Vergnolle, M. Campillo, A. Walpersdorf, N. Cotte, V. Kostoglodov, Slow slip events and strain accumulation in the Guerrero gap, Mexico. *J. Geophys. Res. Solid Earth* **117**, (2012).
26. V. Kostoglodov, S. K. Singh, J. A. Santiago, S. I. Franco, K. M. Larson, A. R. Lowry, R. Bilham, A large silent earthquake in the Guerrero seismic gap, Mexico. *Geophys. Res. Lett.* **30**, 1807 (2003).
27. S. K. Singh, L. Astiz, J. Havskov, Seismic gaps and recurrence periods of large earthquakes along the Mexican subduction zone: A reexamination. *Bull. Seismol. Soc. Am.* **71**, 827–843 (1981).
28. UNAM Seismology Group, Papanoa, Mexico earthquake of 18 April 2014 (Mw7.3). *Geofis. Intern.* **54**, 363–386 (2015).
29. H. Kanamori, P. C. Jennings, S. K. Singh, L. Astiz, Estimation of strong ground motions in Mexico City expected for large earthquakes in the Guerrero seismic gap. *Bull. Seismol. Soc. Am.* **83**, 811–829 (1993).
30. UNAM Seismology Group, The September 1985 Michoacan earthquakes: Aftershock distribution and history of rupture. *Geophys. Res. Lett.* **13**, 573–576 (1986).
31. A. Kato, K. Obara, T. Igarashi, H. Tsuruoka, S. Nakagawa, N. Hirata, Propagation of slow slip leading up to the 2011 M(w) 9.0 Tohoku-Oki earthquake. *Science* **335**, 705–708 (2012).
32. S. Ruiz, M. Metois, A. Fuenzalida, J. Ruiz, F. Leyton, R. Grandin, C. Vigny, R. Madariaga, J. Campos, Intense foreshocks and a slow slip event preceded the 2014 Iquique Mw 8.1 earthquake. *Science* **345**, 1165–1169 (2014).
33. V. M. Cruz-Atienza, J. Tago, C. Villafuerte, M. Wei, R. Garza-Girón, L. A. Dominguez, V. Kostoglodov, T. Nishimura, S. I. Franco, J. Real, M. A. Santoyo, Y. Ito, E. Kazachkina, Short-term interaction between silent and devastating earthquakes in Mexico. *Nat. Commun.* **12**, 2171 (2021).
34. M. Radiguet, H. Perfettini, N. Cotte, A. Gualandi, B. Valette, V. Kostoglodov, T. Lhomme, A. Walpersdorf, E. Cabral Cano, M. Campillo, Triggering of the 2014 Mw7.3 Papanoa earthquake by a slow slip event in Guerrero, Mexico. *Nat. Geosci.* **9**, 829–833 (2016).
35. F. N. Spiess, C. D. Chadwell, J. A. Hildebrand, L. E. Young, G. H. Purcell, H. Dragert, Precise GPS/Acoustic positioning of seafloor reference points for tectonic studies. *Phys. Earth Planet. In.* **108**, 101–112 (1998).
36. Y. Matsumoto, M. Fujita, T. Ishikawa, M. Mochizuki, T. Yabuki, A. Asada, Undersea co-seismic crustal movements associated with the 2005 Off Miyagi Prefecture Earthquake detected by GPS/acoustic seafloor geodetic observation. *Earth Planets Space* **58**, 1573–1576 (2006).
37. J. H. Foster, T. L. Ericksen, B. Bingham, Wave glider–enhanced vertical seafloor geodesy. *J. Atmos. Oceanic Tech.* **37**, 417–427 (2020).
38. C. D. Chadwell, D. A. Schmidt, S. C. Webb, S. L. Nooner, T. L. Ericksen, B. A. Brooks, J. H. Foster, C. D. Chadwell, D. A. Schmidt, S. C. Webb, S. L. Nooner, T. L. Ericksen, B. A. Brooks, J. H. Foster, Expansion of GPS-acoustic arrays offshore the Cascadia and Alaska subduction zones. *American Geophysical Union, Fall Meeting* **2018**, T44C-02 (2018).
39. K. Suzuki, M. Nakano, N. Takahashi, T. Hori, S. Kamiya, E. Araki, R. Nakata, Y. Kaneda, Synchronous changes in the seismicity rate and ocean-bottom hydrostatic pressures along the Nankai trough: A possible slow slip event detected by the Dense Oceanfloor Network system for Earthquakes and Tsunamis (DONET). *Tectonophysics* **680**, 90–98 (2016).
40. A. Polster, M. Fabian, H. Villinger, Effective resolution and drift of paroscientific pressure sensors derived from long-term seafloor measurements. *Geochem. Geophys. Geosyst.* **10**, 8 (2009).
41. R. Hino, T. Kubota, N. Y. Chikasada, Y. Ohta, H. Otsuka, Assessment of S-net seafloor pressure data quality in view of seafloor geodesy. *Prog. Earth Planet Sci.* **9**, 1–18 (2022).
42. J. Gomberg, S. Hautala, P. Johnson, S. Chiswell, Separating sea and slow slip signals on the seafloor. *J. Geophys. Res. Solid Earth* **124**, 13486–13503 (2019).
43. B. He, M. Wei, D. R. Watts, Y. Shen, Detecting slow slip events from seafloor pressure data using machine learning. *Geophys. Res. Lett.* **47**, e2020GL087579 (2020).
44. F. Boudin, P. Bernard, G. Meneses, C. Vigny, M. Olcay, C. Tassara, J. P. Boy, E. Aissaoui, M. Métois, C. Satriano, M. F. Esnoult, A. Nercessian, M. Vallée, J. P. Vilotte, C. Brunet, Slow slip events precursory to the 2014 Iquique Earthquake, revisited with long-base tilt and GPS records. *Geophys. J. Int.* **228**, 2092–2121 (2021).
45. S. Tsuji, E. Araki, T. Yokobiki, S. Nishida, Y. Machida, M. Zumberge, K. Takahashi, Precise tilt measurement by seafloor borehole tiltmeters at the Nankai Trough subduction zone. *Earth Planets Space* **75**, 1–14 (2023).
46. H. Shiobara, A. Ito, H. Sugioka, M. Shinohara, T. Sato, Tilt observations at the seafloor by mobile ocean bottom seismometers. *Front. Earth Sci.* **8**, (2021).
47. A. Iglesias, S. K. Singh, O. Castro-Artola, X. Pérez-Campos, R. D. Corona-Fernandez, M. A. Santoyo, V. H. Espíndola, D. Arroyo, S. I. Franco, A source study of the Mw 7.0 Acapulco, Mexico, earthquake of 8 September 2021. *Seismol. Res. Lett.* **93**, 3205–3218 (2022).
48. D. Melgar, A. Ruiz-Angulo, B. W. Crowell, E. J. Fielding, E. A. Solano-Hernandez, The mechanisms of tsunami amplification and the earthquake source of the 2021 M 7 Acapulco, Mexico, earthquake. *Bull. Seismol. Soc. Am.* **112**, 2902–2914 (2022).
49. H. Gao, M. Liao, G. Feng, An improved quadtree sampling method for insar seismic deformation inversion. *Remote Sens.* **13**, 1678 (2021).
50. J. Tago, V. M. Cruz-Atienza, C. Villafuerte, T. Nishimura, V. Kostoglodov, J. Real, Y. Ito, Adjoint slip inversion under a constrained optimization framework: Revisiting the 2006 Guerrero slow slip event. *Geophys. J. Int.* **226**, 1187–1205 (2021).
51. C. Villafuerte, V. M. Cruz-Atienza, J. Tago, D. Solano-Rojas, R. Garza-Girón, G. Girón, S. I. Franco, L. A. Dominguez, V. Kostoglodov, Slow slip events and megathrust coupling changes contribute to the earthquake potential in Oaxaca, Mexico. *Geophys. J. Int.* **241**, 17–34 (2025).
52. S. K. Singh, R. D. Corona-Fernandez, M. Á. Santoyo, A. Iglesias, Repeating large earthquakes along the Mexican subduction zone. *Seismol. Res. Lett.* **95**, 458–478 (2024).
53. S. E. Graham, C. DeMets, E. Cabral-Cano, V. Kostoglodov, A. Walpersdorf, N. Cotte, M. Brudzinski, R. McCaffrey, L. Salazar-Tlaczani, GPS constraints on the 2011-2012 Oaxaca slow slip event that preceded the 2012 March 20 Ometepec earthquake, southern Mexico. *Geophys. J. Int.* **197**, 1593–1607 (2014).
54. J. R. Davie, C. W. Fenske, S. T. Serocki, Geotechnical properties of deep continental margin soils. *Mar. Georesour. Geotechnol.* **3**, 85–119 (1978).
55. M. A. Hampton, Geotechnical properties of sediment on the Kodiak continental shelf and upper slope, gulf of Alaska. *Mar. Georesour. Geotechnol.* **8**, 159–180 (1989).
56. Y. Okada, Surface deformation due to shear and tensile faults in a half-space. *Bull. Seismol. Soc. Am.* **75**, 1135–1154 (1985).
57. C. DeMets, R. G. Gordon, D. F. Argus, S. Stein, Effect of recent revisions to the geomagnetic reversal time scale on estimates of current plate motions. *Geophys. Res. Lett.* **21**, 2191–2194 (1994).
58. C. DeMets, R. G. Gordon, D. F. Argus, Geologically current plate motions. *Geophys. J. Int.* **181**, 1–80 (2010).
59. W. B. F. Ryan, S. M. Carbotte, J. O. Coplan, S. O'Hara, A. Melkonian, R. Arko, R. A. Weissel, V. Ferrini, A. Goodwillie, F. Nitsche, J. Bonczkowski, R. Zemsky, Global multi-resolution topography synthesis. *Geochem. Geophys. Geosyst.* **10**, 3 (2009).
60. W. B. Frank, N. M. Shapiro, A. L. Husker, V. Kostoglodov, A. A. Gusev, M. Campillo, The evolving interaction of low-frequency earthquakes during transient slip. *Sci. Adv.* **2**, e1501616 (2016).
61. Y. Yamashita, H. Shimizu, K. Goto, Small repeating earthquake activity, interplate quasi-static slip, and interplate coupling in the Hyuga-nada, southwestern Japan subduction zone. *Geophys. Res. Lett.* **39**, (2012).
62. A. Kato, Y. Ben-Zion, The generation of large earthquakes. *Nat. Rev. Earth Environ.* **2**, 26–39 (2020).
63. M. Liu, H. Li, M. Zhang, T. Wang, Graphics Processing Unit-Based Match and Locate (GPU-M&L): An improved match and locate method and its application. *Seismol. Res. Lett.* **91**, 1019–1029 (2020).
64. L. A. Dominguez, T. Taira, V. M. Cruz-Atienza, A. Iglesias, C. Villafuerte, D. Legrand, X. Pérez-Campos, M. Raggi, Interplate slip rate variation between closely spaced earthquakes in Southern Mexico: The 2012 OMETEPEC and 2018 Pinotepa Nacional Thrust Events. *J. Geophys. Res. Solid Earth* **127**, e2022JB024292 (2022).
65. N. Uchida, T. Iinuma, R. M. Nadeau, R. Bürgmann, R. Hino, Periodic slow slip triggers megathrust zone earthquakes in Northeastern Japan. *Science* **351**, 488–492 (2016).
66. M. Nikkhoo, T. R. Walter, Triangular dislocation: An analytical, artefact-free solution. *Geophys. J. Int.* **201**, 1119–1141 (2015).
67. Y. Kaneko, S. B. Nielsen, B. M. Carpenter, The onset of laboratory earthquakes explained by nucleating rupture on a rate-and-state fault. *J. Geophys. Res. Solid Earth* **121**, 6071–6091 (2016).
68. C. Cattania, P. Segall, Precursory slow slip and foreshocks on rough faults. *J. Geophys. Res. Solid Earth* **126**, e2020JB020430 (2021).
69. A. Kato, S. Nakagawa, Multiple slow-slip events during a foreshock sequence of the 2014 Iquique, Chile Mw 8.1 earthquake. *Geophys. Res. Lett.* **41**, 5420–5427 (2014).

70. A. Socquet, J. P. Valdes, J. Jara, F. Cotton, A. Walpersdorf, N. Cotte, S. Specht, F. Ortega-Culaciati, D. Carrizo, E. Norabuena, An 8 month slow slip event triggers progressive nucleation of the 2014 Chile megathrust. *Geophys. Res. Lett.* **44**, 4046–4053 (2017).
71. S. K. Singh, R. Plata-Martínez, X. Pérez-Campos, V. H. Espíndola, D. Arroyo, A. Iglesias, Evidence of directivity during the earthquakes of 8 and 10 May 2014 (M_w 6.5, 6.1) in the Guerrero, Mexico seismic gap and some implications. *J. Seismol.* **23**, 683–697 (2019).
72. J. M. Nocquet, P. Jarrin, M. Vallée, P. A. Mothes, R. Grandin, F. Rolandone, B. Delouis, H. Yepes, Y. Font, D. Fuentes, M. Régnier, A. Laurendeau, D. Cisneros, S. Hernandez, A. Sladen, J. C. Singaucho, H. Mora, J. Gomez, L. Montes, P. Charvis, Supercycle at the Ecuadorian subduction zone revealed after the 2016 Pedernales earthquake. *Nat. Geosci.* **10**, 145–149 (2016).
73. M. Bouchon, D. Marsan, V. Durand, M. Campillo, H. Perfettini, R. Madariaga, B. Gardonio, Potential slab deformation and plunge prior to the Tohoku, Iquique and Maule earthquakes. *Nat. Geosci.* **9**, 380–383 (2016).
74. J. R. Bedford, M. Moreno, Z. Deng, O. Oncken, B. Schurr, T. John, J. C. Báez, M. Bevis, Months-long thousand-kilometre-scale wobbling before great subduction earthquakes. *Nature* **580**, 628–635 (2020).
75. I. Panet, S. Bonvalot, C. Narteau, D. Remy, J. M. Lemoine, Migrating pattern of deformation prior to the Tohoku-Oki earthquake revealed by GRACE data. *Nat. Geosci.* **11**, 367–373 (2018).
76. Y. Dobashi, D. Inazu, Improving detectability of seafloor deformation from bottom pressure observations using numerical ocean models. *Front. Earth Sci.* **8**, (2021).
77. E. K. Fredrickson, J. S. Gomberg, W. S. D. Wilcock, S. L. Hautala, A. J. Hermann, H. P. Johnson, Slow slip detectability in seafloor pressure records offshore Alaska. *J. Geophys. Res. Solid Earth* **128**, (2023).
78. M. Hattab, J. L. Favre, Analysis of the experimental compressibility of deep water marine sediments from the Gulf of Guinea. *Mar. Pet. Geol.* **27**, 486–499 (2010).
79. J. Boussinesq, *Application des Potentiels a l'Etude de le l'Equilibre et du Mouvement des Solides Elastiques* (Gauthier-Villars, 1885).
80. M. Budhu, *Soil Mechanics Fundamentals* (Wiley Blackwell, 2015).
81. G. R. J. Cooper, D. R. Cowan, Comparing time series using wavelet-based semblance analysis. *Comput. Geosci.* **34**, 95–102 (2008).

Acknowledgments: We thank C. Maron, M. Campillo, P. Bernard, L. Seydoux, and T. Nishikawa for enriching discussions. We also thank L. P. Cruz, the Oceanographic Platform Coordination of UNAM, and the crew of the R/V El Puma for all support and efforts. We also thank the crew of the R/V Marcus G. Langseth for support. This research was possible thanks to SATREPS funding from the Japanese government through Kyoto University, from the UNAM through the Institute of Geophysics and the Coordination of Oceanographic Platforms, and from the National Science Foundation of United States of America. **Funding:** This work was supported by Universidad Nacional Autónoma de México, PAPIIT grants IG100617, IG100921, and IN111524; Universidad Nacional Autónoma de México, R/V El Puma grants GGAP2017-1, GGAP2017-2, GGAP2018-1, GGAP2018-2, GGAP2019, GGAP2020, GGAP2023, and GGAP2024; and The Japan Science and Technology Agency–Japan International Cooperation Science and Technology Research Partnership for Sustainable Development, SATREPS grant JPMJSA1510. This research was also supported by NSF grant OCE 20-16062. **Author contributions:** Conceptualization: V.M.C.-A. Methodology: J.T. and V.M.C.-A. Software: V.M.C.-A., J.T., L.R., and L.A.D. Validation: V.M.C.-A., J.T., L.R., E.O.-S., and R.G. Formal analysis: V.M.C.-A. and L.A.D. Investigation: V.M.C.-A., J.T., L.A.D., V.K., Y.I., E.O.-S., T.R.-N., R.G., L.R., A.B., and C.V. Resources: V.M.C.-A., Y.I., J.T., V.K., A.R., S.F., J.R., and E.K. Data curation: V.M.C.-A., L.A.D., S.F., D.S.-R., P.M.-G., E.K., F.B., and J.B.-G. Visualization: V.M.C.-A., L.A.D., A.B., and C.V. Supervision: V.M.C.-A. and Y.I. Project administration: Y.I. and V.M.C.-A. Funding acquisition: Y.I. and V.M.C.-A. Writing—original draft: V.M.C.-A. Writing—review and editing: V.M.C.-A., A.B., J.T., L.A.D., Y.I., T.R.-N., L.R., and C.V. **Competing interests:** The authors declare that they have no competing interests. **Data and materials availability:** Although the data used in this investigation are restricted until the end of 2028 due to confidentiality clauses of the SATREPS-UNAM Mexico-Japan project, because of the policies due to the requirements of the journal, the seafloor pressure and tilt data are accessible at the Zenodo repository under DOI:10.5281/zenodo.15947964 (https://zenodo.org/records/15947964). GPS and broadband seismological data are publicly available on request from Servicio Sismológico Nacional of the UNAM (www.ssn.unam.mx/contacto/) or by contacting contacto@sismologico.unam.mx.

Submitted 22 November 2024
Accepted 12 August 2025
Published 10 September 2025
10.1126/sciadv.adu8259